Journal of Chromatography A, 1218 (2011) 6331–6347

Contents lists available at ScienceDirect

Journal of Chromatography A

journal homepage: www.elsevier.com/locate/chroma

Proline-based chiral stationary phases: A molecular dynamics study of the interfacial structure

M. Ashtari, N.M. Cann*

Department of Chemistry, Queen's University, Kingston, Ontario K7L 3N6, Canada

ARTICLE INFO

Article history:
Received 27 April 2011
Received in revised form 24 June 2011
Accepted 27 June 2011
Available online 3 July 2011

Keywords:
Proline
Molecular dynamics simulation
Chiral stationary phase
HPLC
Normal-phase
Reversed-phase
Chiral chromatography

ABSTRACT

Proline chains have generated considerable interest as a possible basis for new selectors in chiral chromatography. In this article, we employ molecular dynamics simulations to examine the interfacial structure of two diproline chiral selectors, one with a terminal trimethylacetyl group and one with a terminal t-butyl carbamate group. The solvents consist of a relatively apolar *n*-hexane/2-propanol and a polar water/methanol mixture. We begin with electronic structure calculations for the two chiral selectors to assess the energetics of conformational changes, particularly along the backbone where the amide bonds can alternate between cis and trans conformations. Force fields have been developed for the two selectors, based on these *ab initio* calculations. Molecular dynamics simulations of the selective interfaces are performed to examine the preferred backbone conformations, as a function of end-group and solvent. The full chiral surface includes the diproline selectors, trimethylsilyl end-caps, and silanol groups. Connection is made with selectivity measurements on these interfaces, where significant differences [1] are observed between these two very similar selectors.

1. Background

Polyproline chains have been of interest in biology for many years. These chains have a unique backbone structure that consists of amide bonds and rigid pyrrolidine rings and, without hydrogen bond donors, polyproline does not support main-chain hydrogen bonding. Polyproline chains can adopt different conformations. In particular, when the backbone amides are all trans, the structure is known as PPII. The backbone in PPII is a left-handed helix with a pitch of 9.4 Å and 3.0 residues per turn. The all-cis configuration, referred to as PPI, is much more compact with a right-handed helical pitch of 5.6 Å and 3.3 residues per turn. In water, polyproline adopts a PPII structure [2,3]. PPI is known to occur [2–4] for polyprolines solvated by aliphatic alcohols. Structures intermediate to PPI and PPII are also known: recent experimental evidence [5] suggests that PPII structures found in proteins have a number of cis defects, such that the backbone is more compact than expected. Amino acid residues, not necessarily containing proline [6], that cannot adopt an α-helix may alternatively adopt the PPII structure. In fact, a study of the HOMSTRAD database of structurally aligned homologous proteins [5] found that 60% of the protein chains contained at least one PPII helix.

Chiral high performance liquid chromatography (HPLC) is a commonly used technique for separating racemic mixtures [7]. The selector in chiral HPLC is attached to a substrate, either covalently or ionically. In a brush-type chiral stationary phase (CSP), the selective molecule is relatively small, and joined to the substrate via a hydrocarbon tether. Polyproline CSPs have been the subject of considerable interest in the past few years. In 2005, Huang et al. [8], examined diproline and tetraproline selectors and found that tetraproline resolved 31 out of 53 analytes tested. This promising result showed that polyproline CSPs were competitive with the well-known Daicel AD-H, Daicel OD-H and the Whelk O columns [8]. Huang et al. [9] undertook optimization of the polyproline selector by examining the role of the terminal group on the proline chain, specifically by replacing 9-fluorenylmethoxycarbonyl with seven other terminal groups. In 2006, Huang et al. [1] performed a more detailed study of proline chain length by comparing diproline, tetraproline, hexaproline, and decaproline selectors. The nature and length of the tether were also explored. Since then, a number of selectors have been synthesized and examined: Sancho and Minguillon examined a selector containing 3,5-dimethylphenylcarbamate on the 4 position on the pyrrolidine rings [10]; Li et al. attached a diproline chiral selector to polymer to improve selectivity for chiral alcohols and amines [11]; a pentaproline selector was synthesized and examined by Bao et al. [12]; triprolines and tri-α-methylproline selectors were examined by Lao and Gan [13]; the linkage to the surface was explored by Lao and Gan in 2009 [14] by comparing the usual singly attached

* Corresponding author. Tel.: +1 613 533 2651; fax: +1 613 533 6669.
E-mail address: ncann@chem.queensu.ca (N.M. Cann).

0021-9673/$ – see front matter © 2011 Elsevier B.V. All rights reserved.
doi:10.1016/j.chroma.2011.06.096

covalently bonded diproline selector to a covalently bonded doubly tethered selector, and to singly and doubly attached ionically bonded selectors. Collectively, these studies indicate that longer proline chains are typically more selective but that other factors such as tether length, the identity of the terminal group, substitution on the pyrrolidine ring, the type of surface linkage, and the nature of the solvent all impact the selectivity.

To accompany the experimental work on polyproline, a number of computational studies have been reported. Zhong and Carlson [5] explored Ac-$(Pro)_n$-OMe dimers ($n=2$) and hexamers ($n=6$) using B3LYP. They found that the all-trans PPII conformations are favoured in the gas phase. The impact of a continuum solvent, representative of chloromethane, methanol, or water was examined for the hexamer. Their calculations indicate that, contrary to experiment, the PPI conformer is stable in the more polar solvents but explicit hydrogen bonding is not present in their solvation model. Kang et al. [15] performed a similar conformational study on Ac-$(Pro)_n$-NMe_2, $n=2$–5 using Hartree–Fock theory. Their calculations indicate that all-trans PPII conformations are most stable in the gas phase, and in solutions of chloroform, 1-propanol, and water. In contrast, a recent RI-MP2 study by Kuemin et al. [4] suggests that 6-mer, 9-mer, and 12-mers of Ac-$(Pro)_n$-NH_2 and Ac-$(Pro)_n$-OCH_3 prefer the all-cis PPI configuration in the gas phase, except for Ac-$(Pro)_6$-NH_2 where PPI and PPII are found to be isoenergetic.

In this article, we examine diproline at several levels of theory. Specifically, conformers are examined with 2nd order Moller–Plesset (MP2) perturbation theory, coupled-cluster singles and doubles (CCSD) theory, the local pair natural orbital coupled cluster theory (LPNO-CCSD) [16,17], and density functional theory with the B3LYP, the B97D [18], and the MPW2PLYP-D [19–21] functionals. We adopt a broad range of approaches to definitively identify the energetic ordering of the diproline conformers. This breadth also allows some analysis of the impact of dispersion on conformer stability and, in particular, B97D and MPW2PLYP-D are designed to include dispersion corrections. To develop force fields for diproline, we begin with a series of electronic structure calculations to obtain the energy and structure of the conformers. These calculations are performed at the B3LYP, B97D, MPW2PLYP-D, and MP2 levels, with single point energy calculations performed using LPNO-CCSD and CCSD. An assessment of energetic costs for conformational change is required for force field design. However, this assessment requires an extensive series of calculations and only B3LYP and B97D were employed for these calculations. The final force fields are adjusted to be consistent with single point energies obtained with CCSD.

In order to isolate the end-group effect, we examine two diproline selectors, one with a terminal trimethylacetyl (TMA) group and another with a t-butyl carbamate (BOC) group. Although these terminal groups are structurally very similar, we have chosen them since the TMA-terminated diproline is a superior chiral selector to the BOC-terminated selector [9]. For instance, TMA-terminated diproline successfully separates benzoin with a selection factor of 1.14 while the BOC-terminated selector does not distinguish between the benzoin enantiomers [9]. Overall, TMA-$(Pro)_2$-$N(CH_3)_2$ separated 39 of 52 analytes while BOC-$(Pro)_2$-$N(CH_3)_2$ separated only 26 of the analytes and, for the successful separations, gave an average selection factor of only 1.09 [9]. With these considerations, force fields have been independently developed for TMA-$(Pro)_2$-$N(CH_3)_2$ and BOC-$(Pro)_2$-$N(CH_3)_2$. Molecular dynamics simulations are employed to examine the interfacial structure of these two diproline selectors. The model chiral interface includes trimethylsilyl end-caps, silanol groups, and the diproline selectors tethered to the surface with a propyl linkage. For each of the two terminal groups, two solvents are chosen: *n*-hexane/2-propanol and water/methanol. This choice is motivated by the fact that these solvents are used in chromatography and that

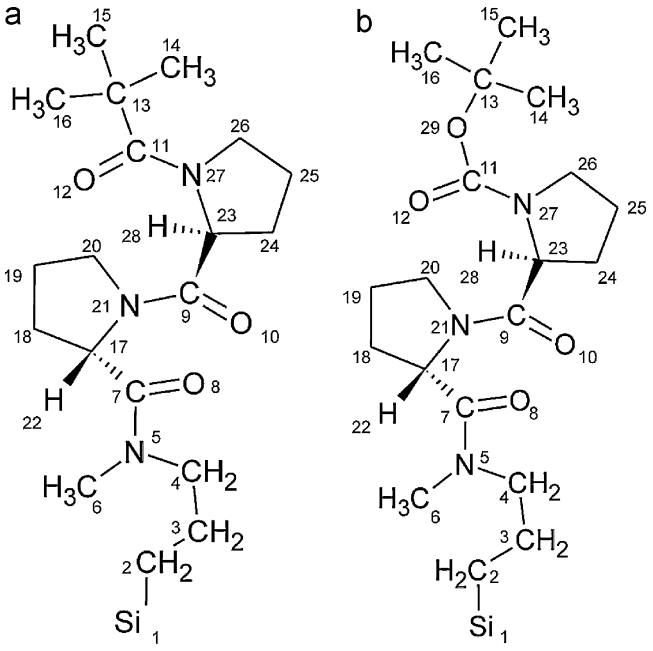

Fig. 1. The two diproline selectors, TMA-$(Pro)_2$-$N(CH_3)$-tether and BOC-$(Pro)_2$-$N(CH_3)$-tether, are shown in (a) and (b) respectively. The atom numbering shown above is used throughout. A single number identifies each methyl and methylene since a united-atom representation is adopted for these groups.

polyproline conformations change from PPI in aliphatic alcohols to PPII in polar solvents [2,3,22]. The conformational distribution of the diproline selectors is monitored during the simulations, with emphasis on the orientation of backbone carbonyl groups. The solvent distribution in the vicinity of the surface is also examined with emphasis on the extent of hydrogen bonding along the backbone.

Stationary phases are uniquely difficult to simulate because they require an atomic level description of a complex interface. An approximation to the distribution of the selector, a large molecule, and other components at the surface is also required. Despite these challenges, simulations of the entanglement and solvation of long chain alkanes tethered to silica have been undertaken [23–26] but only a few simulations of chiral interfaces have been published [27–30]. Aside from simulations, current theoretical methods include force field based exploration of docked complexes [31], and statistical, structure–function approaches aimed at selectivity predictions [32–34].

This article begins with a description of the diproline selectors. Details of the molecular dynamics simulations for the diproline interfaces are also provided in Section 2. Interfacial structure, solvent distributions and hydrogen bonding at the selective interfaces are compared in Section 3. The article concludes with a brief discussion of the results.

2. Theoretical details

The two diproline selectors, TMA-$(Pro)_2$-$N(CH_3)$-tether and BOC-$(Pro)_2$-$N(CH_3)$-tether, are shown in Fig. 1. They differ only in that the latter has an additional oxygen before the terminal t-butyl group. In this section the electronic structure calculations on truncated selectors, TMA-$(Pro)_2$-$N(CH_3)_2$ and BOC-$(Pro)_2$-$N(CH_3)_2$, and the ensuing force fields are discussed in Sections 2.1 and 2.2. The interfacial system is presented in Section 2.3 along with a description of the potential for the solvent–surface interactions. Properties of interest, such as solvent distribution at the interface, are defined in Section 2.4. Computational details are presented in Section 2.5.

Table 1
Conformers TMA-$(Pro)_2$-$N(CH_3)_2$ and BOC-$(Pro)_2$-$N(CH_3)_2$. The first column identifies the conformation about the amide bonds: "TT" ("CC") identifies trans (cis) geometries about C(11)–N(27) and C(9)–N(21); "TC" ("CT") refers to a trans(cis) geometry about C(11)–N(27) and a cis (trans) geometry about C(9)–N(21). Energies, in kJ/mol, are reported relative to the lowest energy conformer for each method. CCSD and LPNO-CCSD single-point calculations are performed for the B3LYP and B97D minimum energy structures. The energies in brackets, for CCSD and LPNO-CCSD, are relative to the overall minimum energy structure. Results are provided for: ΔE^a, B3LYP/6-311G(d,p); ΔE^b, B97D/6-311G(d,p); ΔE^c, MPW2PLYP-D/cc-pVTZ; ΔE^d, MP2/6-311G(d,p); ΔE^e, CCSD/6-311G(d,p)//B3LYP/6-311G(d,p); ΔE^f, CCSD/6-311G(d,p)//B97D/6-311G(d,p); ΔE^g, LPNO-CCSD/6-311G(d,p)//B3LYP/6-311G(d,p); ΔE^h, LPNO-CCSD/6-311G(d,p)//B97D/6-311G(d,p) calculations.

Characteristics	ΔE^a B3LYP	ΔE^b B97D	ΔE^c MPW2PLYP-D	ΔE^d MP2	ΔE^e CCSD//B3LYP	ΔE^f CCSD//B97D	ΔE^g LPNO-CCSD//B3LYP	ΔE^h LPNO-CCSD//B97D
TMA-$(Pro)_2$-$N(CH_3)_2$								
TT	0.0	7.1	0.0	0.0	0.0 (0.0)	0.0 (2.5)	0.0 (0.0)	0.0 (7.4)
TC	17.6	0.0	8.9	6.0	6.7 (6.7)	5.9 (8.4)	4.9 (4.9)	2.9 (9.4)
CT	14.5	10.5	8.8	8.7	8.2 (8.2)	6.3 (8.9)	6.9 (6.9)	4.9 (12.1)
CC	30.8	17.3	22.7	26.2	21.7 (21.7)	20.2 (22.7)	19.7 (19.7)	17.3 (25.2)
BOC-$(Pro)_2$-$N(CH_3)_2$								
TT	0.0	5.4	2.7	2.4	1.9 (1.9)	0.3 (6.6)	0.0 (0.0)	0.0 (6.0)
TC	19.4	0.0	11.3	9.5	10.1 (10.1)	7.5 (13.8)	12.3 (12.3)	8.6 (14.6)
CT	4.2	0.9	0.0	0.0	0.0 (0.0)	0.0 (6.2)	2.1 (2.1)	1.7 (7.7)
CC	23.8	14.0	20.4	16.3	18.9 (18.9)	17.1 (23.4)	19.4 (19.4)	21.1 (27.1)

[a] Relative energies for B3LYP/6-311G(d,p) optimized structures.
[b] Relative energies for B97D/6-311G(d,p) optimized structures.
[c] Relative energies for MPW2PLYP-D/cc-pVTZ optimized structures.
[d] Relative energies for MP2/6-311G(d,p) optimized structures.
[e] CCSD/6-311G(d,p) relative energies for the B3LYP/6-311G(d,p) optimized structures.
[f] CCSD/6-311G(d,p) relative energies for the B97D/6-311G(d,p) optimized structures.
[g] LPNO-CCSD/6-311G(d,p) relative energies for the B3LYP/6-311G(d,p) optimized structures.
[h] LPNO-CCSD/6-311G(d,p) relative energies for the B97D/6-311G(d,p) optimized structures.

2.1. The diproline selectors

The oligomeric polyproline backbone is characterized by the presence of five-membered rings and by the absence of hydrogen bond donors. With these characteristics, the backbone is quite rigid and unable to form intramolecular hydrogen bonds. Two backbone conformations are known experimentally, PPI and PPII, and they differ markedly, with different helicities and pitches [5,35,36]. From a chromatographic perspective, PPI and PPII should display distinct selectivities. This offers the potential for a unique control of selectivity. A number of polyproline-based stationary phases have been synthesized and tested [4,8–14] and chain-length, substitutions on the backbone, end-caps, and tethers all impact the selectivity. Despite this variation, it is clear from extensive comparisons [1,8] with Whelk-O, Chiralpak AD and Chiralpak OD, that polyproline-based selectors are competitive with the most frequently employed, commercially available selectors.

The two diproline-based selectors of interest, TMA-$(Pro)_2$-$N(CH_3)$-tether and BOC-$(Pro)_2$-$N(CH_3)$-tether, can be roughly divided into three components: the tether joining the selector to the surface; the diproline moiety; and the terminal group which differs slightly for the two selectors. As shown in Fig. 1, each tether consists of a propyl chain covalently bonded to the underlying Si surface. This simple representation of the underlying surface is chosen for three reasons. First, the solvent is sterically excluded from the Si layer. In fact, even water is never within 3 Å of the surface. Second, for brush-type chiral selectors, the crucial interactions occur well above the surface. Finally, the atomic details of the underlying silica are unknown but expected to be varied. The terminal group consists of either TMA or BOC, which differ only by an additional oxygen in the latter. The two selectors each have three amide bonds. The first amide bond joins the two proline units, C(17)–N(21)–C(9)–C(23) in Fig. 1, and is important in describing the relative conformations of the backbone. When the amide torsional angle is near zero, the carbonyl group is cis to the alpha carbon C(17). Likewise, an angle near 180° places the carbonyl oxygen trans to the alpha carbon. The PPI and PPII conformations in polyproline chains are distinguished by the cis and trans conformations, respectively, of this amide. The second amide group joins the terminal group to the diproline unit. The third amide bond joins the tether to the diproline and, for this amide, a cis or trans arrangement merely leads to a reorientation of the diproline moiety relative to the surface. In this article, the conformers of diproline will be identified by the orientation of the first two amides: CC and CT both have a cis amide joining the terminal group and a cis or a trans amide, respectively, joining the prolines; TT and TC both have a trans amide joining the terminal group and a trans or a cis amide, respectively, joining the prolines. Pictures of these conformers are shown in Fig. 2. When the amide joining the prolines is trans, the selector is extended but, with a cis amide between the two prolines, the molecular structure is much more compact. A transition from trans to cis on the amide joining the diproline to the end-group has a smaller impact: the end group is simply repositioned.

The TMA terminal group has been chosen for two reasons. First, experiments show [4] that this choice of end group leads to better chiral selectivity, relative to seven other terminal groups. Also, TMA is achiral and relatively small such that its interactions with solvent will be mostly due to H-bonding at the carbonyl oxygen. The BOC terminal group has been selected based on its similarity with TMA and the fact that it is an inferior chiral selector [9]. The elucidation of the reasons for this difference is one of the objectives in this work.

In order to explore the preferred conformations of the two diproline selectors, a series of *ab initio* calculations has been undertaken. Specifically, geometry optimizations are performed for B3LYP/6-311G(d,p), B97D/6-311G(d,p), MPW2PLYP-D/cc-pVTZ and MP2/6-311G(d,p) calculations while single point calculations are performed for the CCSD/6-311G(d,p), and LPNO-CCSD/6-311G(d,p) methods and the optimized B3LYP and B97D structures. The LPNO-CCSD and MPW2PLYP-D calculations are performed using ORCA [37]. All other calculations use Gaussian 09 [38]. The calculations are performed on truncated versions of the selectors, TMA-$(Pro)_2$-$N(CH_3)_2$ and BOC-$(Pro)_2$-$N(CH_3)_2$, where the tether has been replaced by a methyl group. For each truncated selector, geometry optimizations proceed from roughly twenty starting structures to find the lowest energy gas phase conformers. Results are presented in Table 1.

Previous *ab initio* studies [4,5,15] have been reported for the proline dimer but they disagree. Specifically, Kang et al. [15] used HF/6-31+G(d) to find minima for CH_3CO-$(Pro)_2$-$N(CH_3)_2$ dimer: the lowest energy minima are TT, followed by CT, and CC. In contrast,

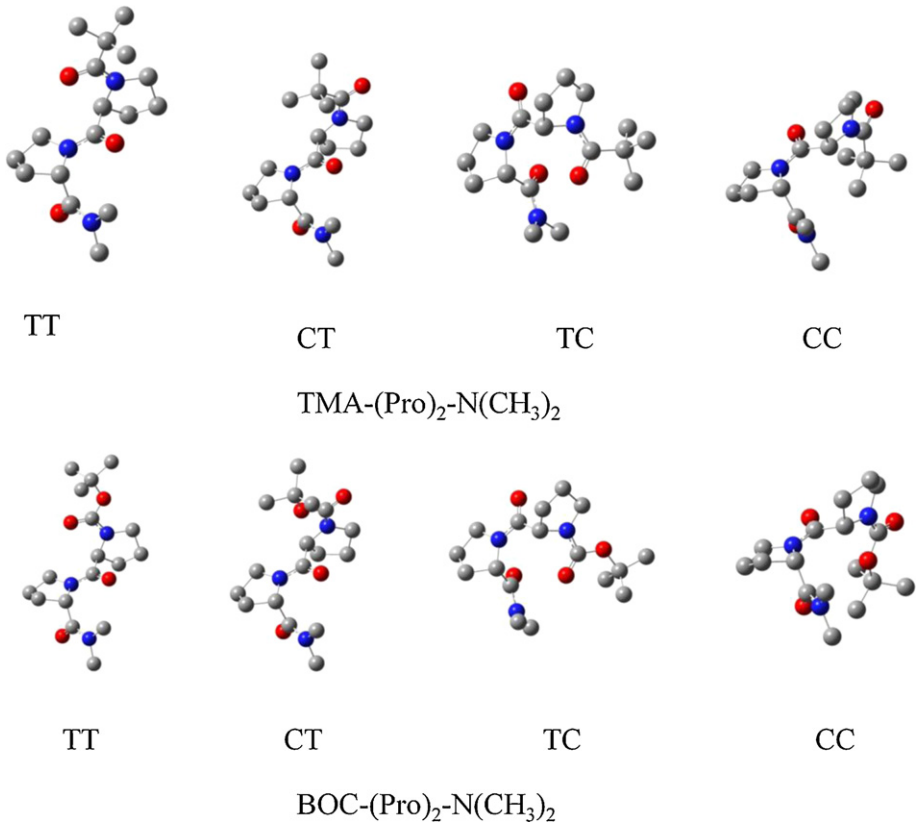

Fig. 2. Stable conformers from B3LYP/6-311G(d,p) calculations of TMA-$(Pro)_2$-$N(CH_3)_2$ and BOC-$(Pro)_2$-$N(CH_3)_2$. Note that the tether is replaced by CH_3 for the *ab initio* calculations. The conformers are identified by the torsional angle of the inter-ring and ring-terminal group amide bonds: the TT conformer has two trans amides; CT has a cis amide bond between the proline and TMA with a trans bond between the rings; TC corresponds to a trans proline-TMA amide and a cis torsion between the rings; and two cis amides correspond to CC.

Zhong and Carlson [5] explored a slightly different dimer, CH_3CO-$(Pro)_2$-$NH(CH_3)$, using the B3LYP/6-31G(d) method but they did not identify any CT or TC local minima. In both cases, a PPII conformation was identified as the most stable in the gas phase. Although Kuemin et al. [4] did not examine the dimer, their RI-MP2/SVP calculations yield results in better overall agreement with experiment. Given the difference between the results of previous theoretical calculations, we have obtained the lowest-energy structures at various levels of theory.

The energies in Table 1 illustrate the difficulty in predicting diproline stability. Of the methods chosen, CCSD will capture more of the correlation energy and provides a reference point for assessing the other approaches. The other methods are less computationally demanding than CCSD and should remain feasible for longer chains. B3LYP does not account for dispersion and, for this reason, overestimates the energy gap between conformers. In contrast, MPW2PLYP-D, a dispersion-corrected double-hybrid density functional, predicts the correct conformational sequence. B97D, which adopts the generalized gradient approximation (GGA) B97 functional with an added dispersive correction, overestimates the stabilization from dispersion. In fact, the lowest energy conformer is predicted to be TC, in contrast to all other approaches which indicate that TT is most stable. Aside from B3LYP and B97D, the methods are in reasonable agreement. For the TMA-terminated selector, the conformers increase in energy according to TT < TC ≈ CT < CC. The replacement of TMA with BOC leads to CT ≈ TT < TC < CC. Thus, the addition of an oxygen to the end-group has a dramatic effect: the conformers are closer in energy and the CT conformer is now predicted to be very close in energy to TT (their energies are equal within error).

The pyrrole rings can be up or down, depending on the position of the ring atoms relative to the carbonyl group. Specifically, for diproline, a plane can be defined by C(17)–N(21)–C(20) for the first ring. If C(19), a ring carbon, and C(7), the carbonyl oxygen, are on the same side (both above or both below) of the ring, then the ring is identified as “down”. If they are on opposite sides, the ring is up. The atoms C(23)–N(27)–C(26) define a plane for the second ring. Likewise, the ring is “down” if the ring atom C(25) and the carbonyl carbon C(9) are on the same side of the plane. Otherwise, it is up. Previous theoretical studies [5] have shown that the energy difference per ring inversion is relatively small, generally between 1 and 5 kJ/mol. The structural changes that accompany a ring flip are small and, in particular, we have found that the backbone remains largely unchanged. For these reasons, our force fields are developed for the “down” configuration of the rings.

2.2. Force fields for the diproline selectors

Independent force fields have been developed for BOC-$(Pro)_2$-$N(CH_3)$-tether and TMA-$(Pro)_2$-$N(CH_3)$-tether based on *ab initio* calculations. Specifically, model development follows the procedure outlined below with the force field extracted from B3LYP/6-311G(d,p) calculations. However, the parameters are adjusted to yield an energy difference between conformers that is consistent with CCSD calculations (see Table 1). For comparison purposes, we also repeat the process to develop models based on a series of B97D/6-311G(d,p) calculations. All force field parameters are provided in Supplemental materials.

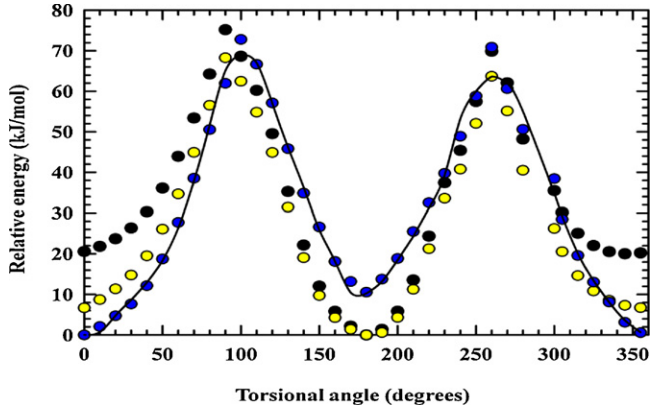

Fig. 3. Torsional barriers for rotation about the inter-ring amide torsion [C(17)–N(21)–C(9)–C(23)] are shown for TMA-$(Pro)_2$-$N(CH_3)_2$. Black circles identify the initial B3LYP/6-311G(d,p) energies. Yellow circles identify the CCSD-corrected torsional potential where the B3LYP energies have been scaled to yield the CCSD cis/trans energy difference from Table 1. Blue circles include corrections for Lennard–Jones and electrostatic interactions between atoms separated by more-than-three bonds. The final torsional potential, obtained by least squares fitting, is shown by a solid line. (For interpretation of the references to color in this figure legend, the reader is referred to the web version of the article.)

The energetic cost for intramolecular changes is given by

$$U^{intra} = U^{stretch} + U^{bend} + U^{improper} + U^{torsion} + U^{NB} \quad (1)$$

where $U^{stretch}$ is the bond stretching potential, U^{bend} accounts for the energetic costs of angle changes, $U^{improper}$ incorporates the energetic costs for out-of-plane motions, the energy associated with twisting about bonds is captured by $U^{torsion}$, and U^{NB} is a non-bonding term between atoms that are separated by four or more bonds. Within the force field, a united-atom representation is adopted for all methyl and methylene groups. As well, the pyrrolidine rings are kept rigid.

Bond stretching is included only between the carbonyl carbons and the adjoining alpha carbons and nitrogens. From Fig. 1, these bonds connect the pyrrolidine rings to the backbone. All other selector bonds are kept fixed using the Rattle algorithm [39]. To account for the energetic cost of changing a bond, a series of ten single point calculations is performed, with the bond length varied by up to ±0.075 Å about the equilibrium value. The resulting energies are least squares fitted to a harmonic potential

$$U^{stretch} = \sum_s k_s(r - r_{e;s})^2 \quad (2)$$

where the sum runs over all the flexible bonds, $r_{e;s}$ is the equilibrium bond length for bond "s", and k_s is the corresponding force constant.

The force field includes potentials for all bends except those that involve three ring atoms, since the rings are rigid in our model. The bending potentials are calculated by sequentially varying each angle about the equilibrium value, in steps of 2.0° up to 10.0°. The bending potential is

$$U^{bend} = \sum_b k_b(\theta - \theta_{e;b})^2 \quad (3)$$

where $\theta_{e;b}$ and k_b are the equilibrium angle and the bending force constant, respectively, for bend "b".

Improper torsions are included to properly account for the energetics of distortion about a central atom. Specifically improper torsion at the alpha carbons, the carbonyl oxygens, and the ring nitrogens are included in the potential. A series of *ab initio* calculations is undertaken with the central atom moving up or down

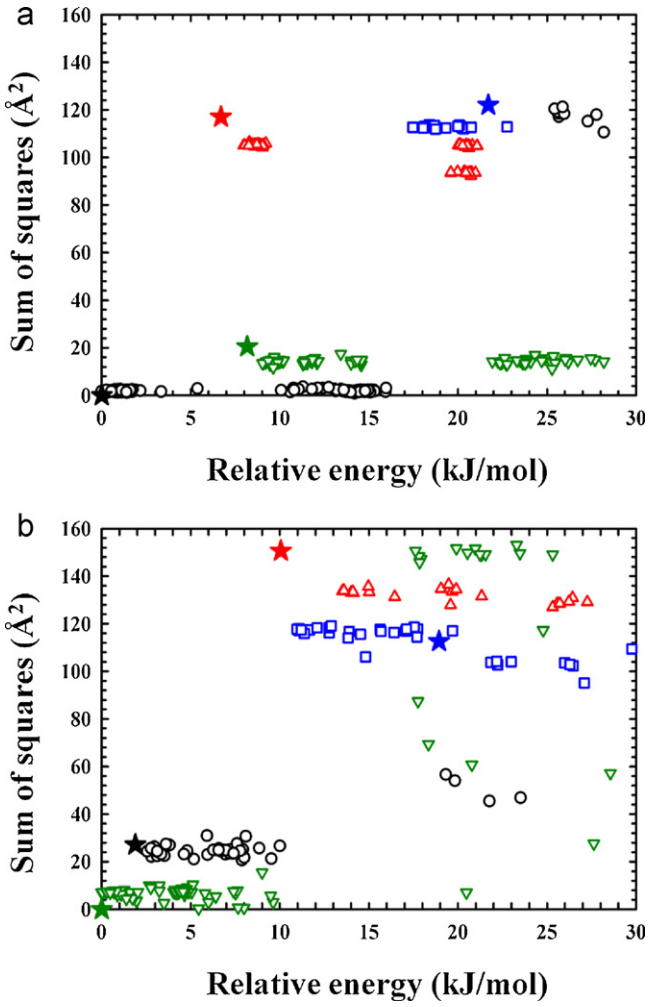

Fig. 4. Force field assessment for TMA-$(Pro)_2$-$N(CH_3)_2$ and BOC-$(Pro)_2$-$N(CH_3)_2$ are shown in (a) and (b) respectively. Each symbol represents a final conformer and its energy, obtained from a single-molecule molecular dynamics simulation. Black circles, green triangles, red triangles, and yellow squares correspond to TT, CT, TC, and CC structures, respectively. The energy of the structure, as predicted from the molecular model, is plotted against the sum of squares, calculated relative to the optimized minimum energy structure obtained for B3LYP/6-311G(d,p) calculations. The open stars identify the relative energies (calculated with CCSD/6-311G(d,p)//B3LYP/6-311G(d,p)) and sum of squares evaluated for the four B3LYP/6-311G(d,p) minimum energy conformers. (For interpretation of the references to color in this figure legend, the reader is referred to the web version of the article.)

relative to the plane of the adjacent three atoms, by as much as 10.0°, in steps of 2.0°. The improper torsion potential has the form

$$U^{improper} = \sum_{it} k_{it}(\omega - \omega_e)^2 \quad (4)$$

where, for three atoms ABC around a central atom D, ω is the angle between the ABC plane and the BCD plane. ω_e is the equilibrium angle and k_{it} is the force constant for the *i*tth improper torsion.

The torsion potential accounts for the energetic changes that accompany twisting about a bond and has the form

$$U^{torsion} = \sum_t \sum_{i=0}^{6} c_{it}(\cos(\varphi_t + \varphi_t^{i;0}))^i \quad (5)$$

where each torsion "*t*" is represented by a cosine series and each term in the series may have a distinct phase shift $\varphi_t^{i;0}$ [40]. This form of the potential is flexible enough to reproduce the energy variation with torsional angle for the entire 360° range of motion.

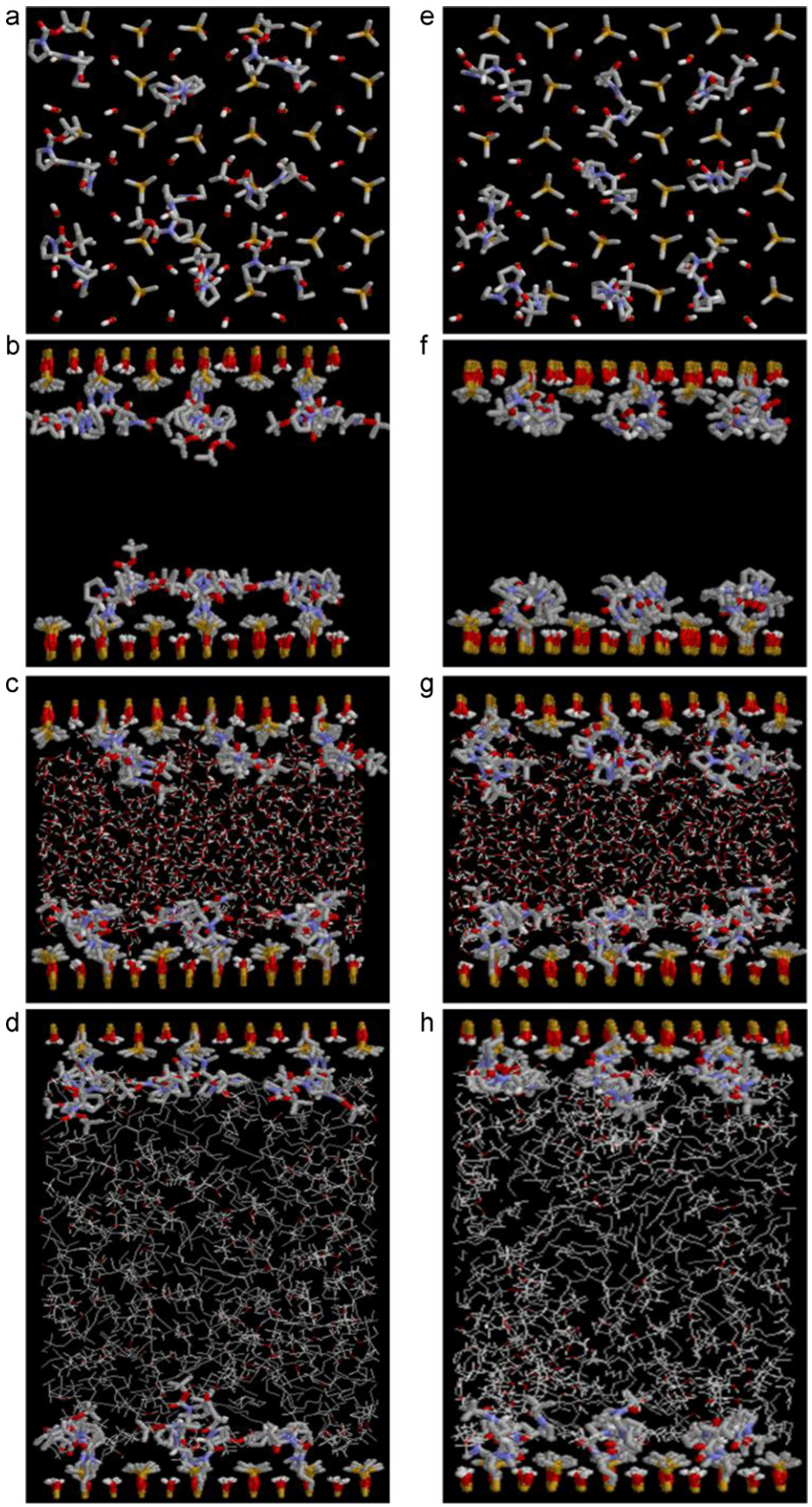

Fig. 5. Illustrative snapshots of the BOC-$(Pro)_2$-$N(CH_3)$-tether interface is shown (a) top view of the surface in the presence of a *n*-hexane/2-propanol solvent, (b) in the absence of solvent, (c) in the presence of a water/methanol solvent and (d) in the presence of a *n*-hexane/2-propanol solvent. Corresponding snapshots of the TMA-$(Pro)_2$-$N(CH_3)$-tether interface are shown in (e)–(h). The underlying Si layer is omitted from the top-views for clarity. Carbon, nitrogen, hydrogen, oxygen, and silicon atoms are shown in grey, blue, white, red, and yellow, respectively. The surfaces include diproline selectors, trimethylsilyl end-caps, silanol groups, and underlying Si atoms. (For interpretation of the references to color in this figure legend, the reader is referred to the web version of the article.)

For each torsion, *ab initio* energies are obtained for a series of 36 angles between 0° and 360°.

Atoms separated by four or more bonds do not share stretch, bend, improper torsion, or torsion potential. Nonetheless some interaction is present between distant, intramolecular atoms. It is customary to introduce "non-bonding" potentials between these atomic pairs but to reduce the potential when transitioning between the close atom regime and the distant atom regime. With these considerations in mind, the non-bonding potential has the form:

$$U^{NB} = C \sum_{\{\geq 4\,bonds\}} 4\varepsilon_{ij}\left[\left(\frac{\sigma_{ij}}{r_{ij}}\right)^{12} - \left(\frac{\sigma_{ij}}{r_{ij}}\right)^{6}\right] + D \sum_{\{\geq 4\,bonds\}} \frac{q_i q_j}{r_{ij}} \qquad (6)$$

where the first sum is a Lennard–Jones (LJ) potential and the second is the electrostatic potential. The constants C and D are unity except for atoms separated by exactly four bonds, where C and D are less than one. Transferrable force fields typically transition between the two regimes when atoms are separated by three bonds. In our previous work [27,28] on phenylglycine- and leucine-based chiral selectors, we also introduced partial non-bonding interactions between 1 and 4 atomic pairs. Here, due to the small differences between conformer energies, we have chosen to introduce non-bonding interactions beginning with 1–5 pairs. Aside from the two parameters, C and D, the "non-bonding" potential is calculated as though the atoms belonged to distinct molecules. The Lennard–Jones parameters in Eq. (6) are taken from the OPLS force field [41–43] while the atomic charges are obtained from the CHELPG algorithm [44] applied to the most stable conformer (TT for B3LYP and TC for B97D).

The evaluation of $U^{torsion}$ is considerably more difficult than an assessment of energetic cost of bending, stretching, or improper torsion. For the latter three, least squares fitting leads directly to the parameters required for Eqs. (2)–(4). Three factors are incorporated into our fitting process for $U^{torsion}$: the torsional angles are coupled such that a change in one angle may lead to a significant change in a nearby torsion; the B3LYP torsion potential is adjusted to be consistent with CCSD energies; non-bonding interactions change with torsional angle and, in order to avoid double counting of non-bonding in the force field, the torsion potential must be adjusted. Details on the incorporation of these three factors are provided in Supplemental materials. Fig. 3 shows their impact on the torsional potential for the inter-ring amide torsion of TMA-$(Pro)_2$-$N(CH_3)_2$.

The proper conformational balance between diproline backbone configurations (TT, CT, TC, and CC) is essential for our simulations. We parameterize our models to accurately reproduce the *ab initio* energies for bond stretching, bending, improper torsion, and torsions. However, a final parameterization step – the optimization of C and D in Eq. (6) – is introduced to optimize the force field. For long, flexible molecules, this final adjustment of the model is important as was shown for leucine- and phenylglycine-based stationary phases [27,28]. Details of the selection of C and D are provided in Supplemental materials.

Fig. 4 shows the final model assessment for TMA-$(Pro)_2$-$N(CH_3)_2$ and BOC-$(Pro)_2$-$N(CH_3)_2$. Each point in the figure corresponds to the relative energy and sum of squares obtained from a single-molecule MD simulation. The simulation starts from a random structure and is performed as the temperature is gradually lowered from 298 to a few degrees Kelvin. The lowest-energy structure obtained in the simulation is kept and analyzed. If the force field accurately predicts the presence and energies of the four conformers, then these single-molecule simulations should converge to the *ab initio* results. As shown in Fig. 4, for both selectors, the force field reproduces the relative energy and structure of the global energy minimum and the lowest-energy conformer. The second lowest energy conformer is generally well represented but, for the highest energy conformer (CC) the structure is well reproduced but the energy is 5–10 kJ/mol too low. However, the force field still predicts that the CC conformer is much higher in energy than the global minimum.

In the end, we obtain models for the diproline chiral selectors that are structurally and energetically consistent with *ab initio* optimized structures. Importantly, our models also reproduce the energetic cost for stretching, bending, twisting about a bond, and out-of-plane motion.

2.3. The chiral interface

Fig. 5 provides illustrative snapshots of the TMA-$(Pro)_2$-$N(CH_3)$-tether and BOC-$(Pro)_2$-$N(CH_3)$-tether interfaces in the absence of solvent, in water/methanol, and in *n*-hexane/2-propanol. Each simulation cell has empty space beyond the two interfaces, such that roughly two thirds of the cell is empty. The empty space allows for the use of 3D periodic boundary conditions. The solvent in our simulations is effectively confined between two infinite, planar chiral surfaces. In the snapshots of Fig. 5, the surfaces are 34.2 Å apart in water/methanol and 63.1 Å apart in *n*-hexane/2-propanol. Although the chiral selectors are regularly distributed on the surface, a 1.10 μmol/m^2 coverage is chosen to be consistent with experiment [45]. The surface also includes 54 trimethylsilyl end-caps, 72 silanol groups with coverages of 3.20 and 4.26 μmol/m^2, respectively, and 144 silicon atoms. Experimental surface distributions of selectors, end-caps, and silanols, are expected to be irregular but, assuming that each selector acts individually, the distribution on the surface should have minimal impact for a brush-type chiral stationary phase. The underlying, immovable layer of silicon atoms, shown in yellow in Fig. 5, is a simple cubic lattice with atoms 3.12 Å apart.

The energy of the interfacial system is given by:

$$E^{full} = \frac{1}{2}\sum_i m_i v_i^2 + \frac{1}{2}\sum_{RU} I_{RU}\omega_{RU}^2 + U^{LJ} + U^{electro} + U^{intra} \qquad (7)$$

where U^{intra} is the intramolecular potential discussed in Section 2.2. The first term in Eq. (7) is the translational kinetic energy while the second term is the rotational kinetic energy. The latter is calculated for the rigid pyrrolidine ring units (*RU*) in the selectors. The translational kinetic energy includes contributions from the solvent, the end-caps, the silanol groups, and the selectors but the underlying Si layer is immoveable and does not contribute. For the selectors, only the centers of the pyrrolidine rings contribute to the translational kinetic energy. m_{RU} is the mass of the ring, I_{RU} and ω_{RU} are the moments of inertia and angular velocity, respectively, in the principal coordinate system of the ring.

Interactions between the surface and solvent, between solvent components, and between surface-bound molecules are represented by Lennard–Jones and electrostatic potentials. The former is

$$U^{LJ} = \sum_{atom\,pairs,i,j} 4\varepsilon_{ij}\left[\left(\frac{\sigma_{ij}}{r_{ij}}\right)^{12} - \left(\frac{\sigma_{ij}}{r_{ij}}\right)^{6}\right] \qquad (8)$$

where ε_{ij} and σ_{ij} are the well depth and size parameters, respectively, and r_{ij} is the interatomic separation. For the surface components, OPLS [41–43] parameters are chosen except for Si where CHARMM values are employed [46]. LJ parameters for *n*-hexane, 2-propanol and methanol are obtained from Ref. [47]. The flexible F3C water model [48] has been adopted.

Electrostatic interactions are also included. Specifically, for our simulations the selectors, the 2-propanol, the methanol, and the

water have atoms that bear partial charges. The electrostatic potential is

$$U^{electro} = \sum_{atom\ pairs, i,j} \frac{q_i q_j}{r_{ij}} \quad (9)$$

where q_i is the partial charge on atom i. Literature values [47,48] have been adopted for the solvent atomic charges.

2.4. The assessment of interfacial structure

The assessment of interfacial structure begins with surface distribution functions. These distributions are obtained from

$$g(z) = \frac{n^{actual}(z)}{n^{ideal}(z)} \quad (10)$$

where $n^{actual}(z)$ is the number of atoms found between z and $z + \Delta z$ from the underlying Si layer, and $n^{ideal}(z)$ is the number expected for an unstructured, random distribution. In this way, $g(z)$ identifies areas of concentration and depletion for each atom above the surface. For solvent distributions, the number of solvent molecules expected at a distance z above the surface is $n^{ideal}(z) = \rho \Delta z L_x L_y$ where L_x and L_y are the surface dimensions, and ρ is the density. For surface distributions, we have a total of N_s surface atoms and $n^{ideal}(z) = N_s/100$ where the distance between the surfaces has been divided into one hundred segments ($L_z/\Delta z = 100$). The surface $g(z)$ distributions integrate to N_s. Since the simulation cell includes two identical surfaces, the two surface distributions are averaged in the results reported below.

Detailed information of solvent location at the interface is provided by 2-dimensional (2D) cylindrical distributions $g(r_c,z_c)$. In this case, interatomic separations are divided into a component perpendicular to the surface, z_c, and a component parallel to the surface, r_c. These 2D distributions are used to study the relative positions of chosen solvent atoms around the chiral selector.

$$g(z_c, r_c) = \frac{n_{actual}(z)}{n_{ideal}(z)} = \frac{n^{actual}(z)}{2\pi r_c \Delta r_c \Delta z_c \rho} \quad (11)$$

where ρ is the number density of the solvent, and $\Delta r_c = \Delta z_c = 0.094$ Å for n-hexane/2-propanol and $\Delta r_c = \Delta z_c = 0.107$ Å for water/methanol. A positive z_c means the solvent atom is located above (further from the underlying Si layer) the surface atom. 2D distributions are particularly instructive for hydrogen bonding interactions between solvent and selector.

Snapshots of the interfacial system provide direct confirmation of the selector conformations and solvent–selector interactions. The occurrence of hydrogen bonding is detected from the snapshots via the application of a geometric criterion [49,50]: the distance between H and hydrogen bond acceptor should be less than 2.6 Å; the distance between the H-bond donor and H-bond acceptor should be less than 3.5 Å; and the angle formed between donor-H-acceptor should be larger than 150°. We analyze hydrogen bonding probabilities for both selectors and for the amide oxygens and amide nitrogens in the backbone. The orientation of selector carbonyl groups is also analyzed from the snapshots. In this case, the angle between the C=O bond and the surface normal is averaged and results are reported.

2.5. Simulation details

Extensive molecular dynamics (MD) simulations were performed for the chiral surfaces in the presence of a vacuum, a 70/30 (v/v) n-hexane/2-propanol solvent and a 70/30 (v/v) water/methanol solvent. These specific solvent mixtures have been chosen since they are commonly employed for chiral separations, although the amount of co-solvent varies depending on the analyte. The surfaces include end-caps, silanol groups, and a layer of immoveable silicon with coverages that are consistent with experiment [45]. In practice, for the simulations, the intersurface distance is adjusted such that the solvent density in the center of the simulation cell is within 2% of the experimental density. This adjustment is required because the volume occupied by silanol groups, diproline selectors, and end-caps cannot be exactly estimated. For the n-hexane/2-propanol simulations, the surfaces are 63.1 Å apart the simulation cell includes 231 n-hexane molecules and 169 2-propanol molecules, consistent with the experimental solvent density [51] at 298 K. The water/methanol solvent is denser [52] and, with 645 water molecules and 155 methanol molecules in the simulation cell, the surfaces are 34.2 Å apart. In all cases, each surface includes 9 selectors and has a surface area of 1177.86 Å^2.

Ewald summations [53] have been used to treat the electrostatic forces between partially charged atoms. The empty space beyond the chiral surfaces along with a correction for the elongated shape of the simulation cell [54], allow the use of 3D Ewald sums. An Ewald convergence parameter of $\alpha = 1.756/L_x$ was chosen for all simulations, with a reciprocal space cutoff of $k^2 \leq 27$.

Simulations are performed in the canonical ensemble (NVT) with the use of two Nosé–Hoover thermostats [55,56]. One thermostat is applied to translational motion while the other maintains the rotational temperature of the rigid rings. All simulations are performed at 298 K. The conserved quantity within the simulations is:

$$H_{NH} = E^{full} + \frac{Q_t \varsigma_t^2}{2} + g_t k_B T \ \ln s_t + \frac{Q_t \varsigma_r^2}{2} + g_r k_B T \ \ln s_r \quad (12)$$

where the total energy, E^{full}, is given in Eq. (7). The two additional degrees of freedom, s_t for translation and s_r for rotation, have masses of Q_t and Q_r, respectively, velocities of ς_t and ς_r, and g_t and g_r degrees of freedom. The translational equations of motion are integrated following the algorithm of Martyna et al. [57] to preserve the Rattled [39] positions and velocities. The ring quaternions are advanced in time by coupling a leap-frog algorithm with a Newton–Raphson based scheme for the angular velocity and ς_r.

For each solvent/surface combination, ten molecular dynamics simulations of roughly 0.8 ns duration have been performed for a total simulation time of around 8.0 ns. The time step in the simulations is 0.3 fs, and the simulations are performed with the MDMC program [58] which includes a parallel implementation of the electrostatic and Lennard–Jones force calculations. The equilibration period extends over the first 500,000 time steps of each simulation, leaving a 2,100,000 step collection period. With this time step, H_{NH} is relatively constant with long-term drift of around 2.0 kJ/mol during the collection period of the simulation. The equilibrium properties reported in Section 3 are averages over twenty surfaces (2 surfaces/simulation and ten simulations per solvent).

Initial configurations are generated by placing each selector in the minimum energy configuration (TT for TMA-$(Pro)_2$-$N(CH_3)$-tether and CT for BOC-$(Pro)_2$-$N(CH_3)$-tether). As shown in Fig. 3, the barrier for interconversion between cis and trans amide bonds is roughly 70 kJ/mol. Such a barrier is not expected to be overcome at 298 K. We have allowed for equilibration of the three amide bonds in the selectors by introducing a time-dependent scaling function that temporarily lowers the barrier to amide cis/trans interconversion without altering the relative energies of the conformers. Specifically, the amide torsions are represented by

$$U^{torsion}(\varphi_t, t) = S(\varphi_t, t) \sum_{i=0}^{6} c_{it} (\cos(\varphi_t - \varphi_t^{i;0}))^i \quad (13)$$

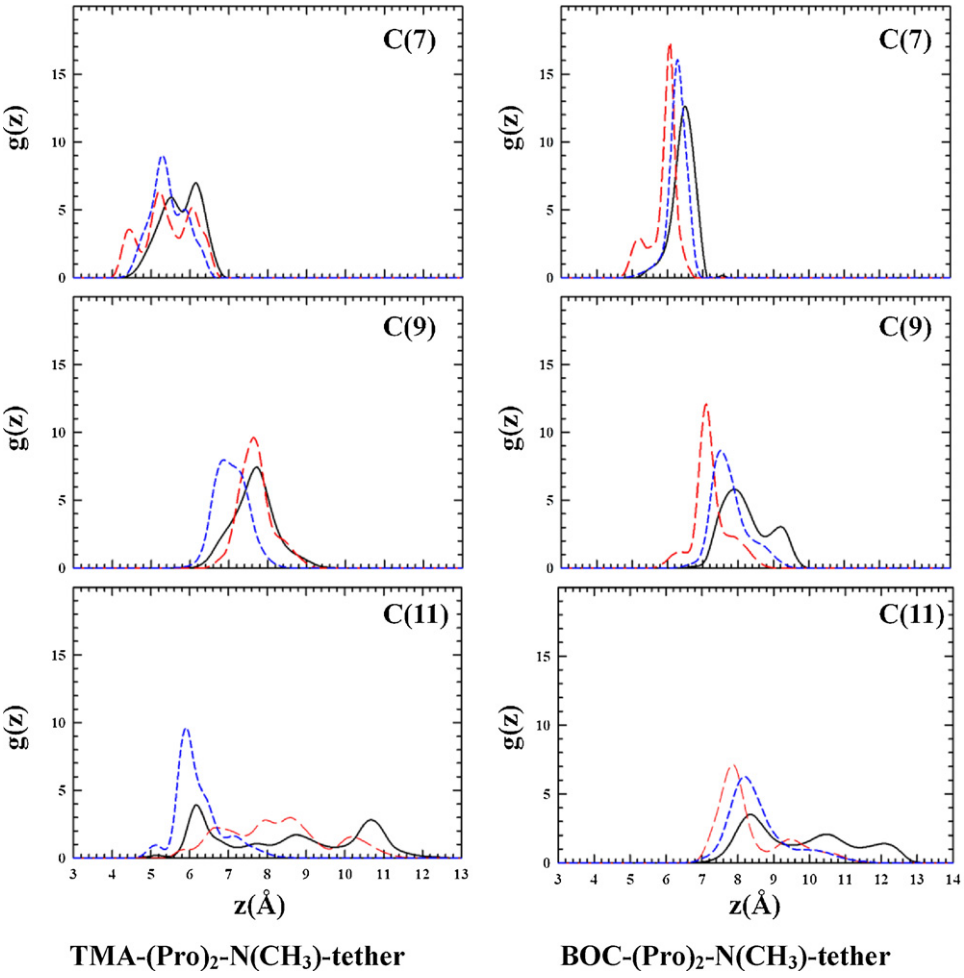

Fig. 6. Surface distributions of carbonyl carbons (see Fig. 1 for atom numbering) for the TMA-$(Pro)_2$-$N(CH_3)$-tether and the BOC-$(Pro)_2$-$N(CH_3)$-tether selector. Results are shown in the absence of solvent (blue, short dashes), in *n*-hexane/2-propanol (black, solid), and in water/methanol (red, long dashes). (For interpretation of the references to color in this figure legend, the reader is referred to the web version of the article.)

where

$$S(\varphi_t, t) = \frac{(t - 3\,\text{ps}) + (60\,\text{ps} - t\,\cos^2\,\varphi_t)}{57\,\text{ps}}$$

for simulations between 3 ps and 60 ps. At other times, the scaling function is one. A further 90 ps of equilibration follows the "scaling in" of the amide torsional barrier. It is important to note that the amide conformational balance is obtained in the presence of solvent and other surface elements such as end-caps.

The results presented in Section 3 are obtained using the CCSD-corrected B3LYP-based force fields. Although B97D force fields were also obtained, and simulations conducted, we do not report results here for the following reasons. The B97D functional predicts TC conformers of TMA-$(Pro)_2$-$N(CH_3)_2$ and BOC-$(Pro)_2$-$N(CH_3)_2$ that differ structurally from the B3LYP, MP2, and MPW2PLYP-D structures. In fact, the latter three methods always predict comparable minimum energy structures (dihedral angles are within 5° for example). Further, as shown in Table 1, CCSD calculations indicate that the B97D TC structures are roughly 2–4 kJ/mol higher in energy than the TC conformers predicted from the other methods. Thus, the B97D functional is not consistent with other methods, and CCSD calculations confirm that B97D predicts incorrect TC structures.

Table 2
Conformational preferences of TMA-$(Pro)_2$-$N(CH_3)$-tether and BOC-$(Pro)_2$-$N(CH_3)$-tether at the interface. The percentage of selectors adopting the specific conformer is given. "TT" identifies trans geometries about C(11)–N(27) and C(9)–N(21); "TC" ("CT") refers to a trans(cis) geometry about C(11)–N(27) and a cis (trans) geometry about C(9)–N(21); TG(T) and TG(C) have a trans geometry about C(11)–N(27) and a gauche geometry about C(9)–N(21) with the latter either close to cis (TG(C)) or close to trans (TG(T)).

Termi-nal group	Solvent	TT	TC	CT	TG(T)	TG(C)	Other
TMA	None	2	18	0	7	67	6
	Water/methanol	43	30	0	2	25	0
	n-Hexane/2-propanol	54	5	5	10	24	2
BOC	None	69	12	17	2	0	0
	Water/methanol	14	1	85	0	0	0
	n-Hexane/2-propanol	25	5	69	0	1	0

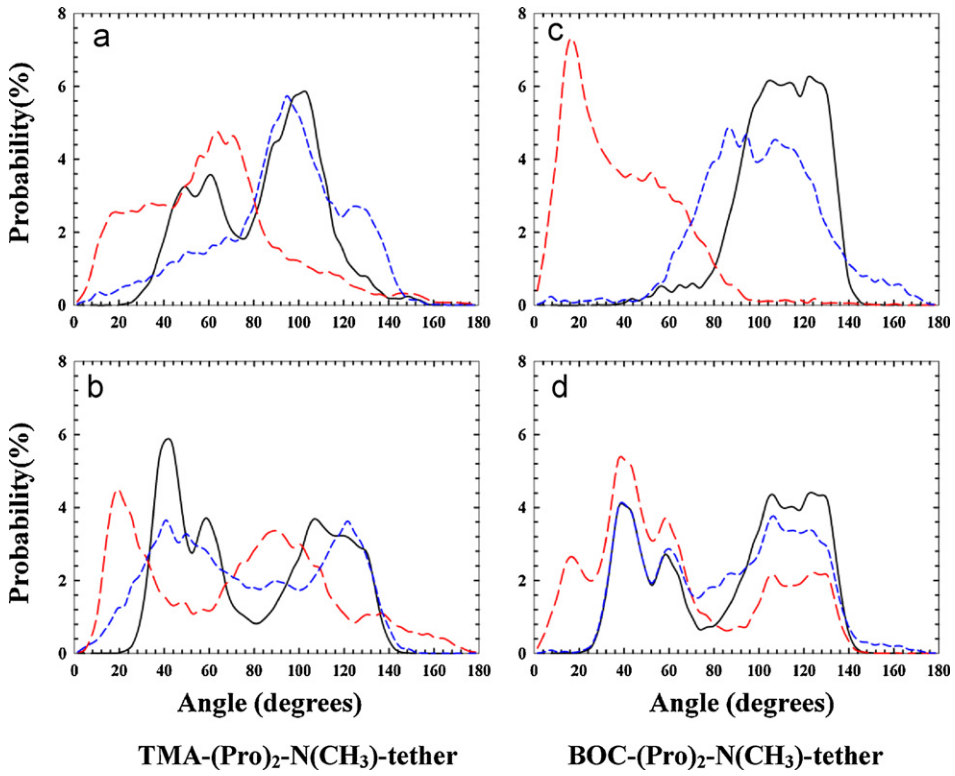

Fig. 7. The distribution of carbonyl orientations at interface. Results are given for (a) *n*-hexane/2-propanol at the TMA-$(Pro)_2$-$N(CH_3)$-tether interface, (b) water/methanol at the TMA-$(Pro)_2$-$N(CH_3)$-tether interface, (c) *n*-hexane/2-propanol at the BOC-$(Pro)_2$-$N(CH_3)$-tether interface, and (d) water/methanol at the BOC-$(Pro)_2$-$N(CH_3)$-tether interface. The percentage of carbonyls with the given angle relative to the Si layer is shown: an angle of 0° corresponds to the carbonyl pointing directly at the underlying Si layer. Distributions for O(8), O(10), and O(12) are represented by (black, solid), (red, long dashed), and (blue, short dashed) lines, respectively. (For interpretation of the references to color in this figure legend, the reader is referred to the web version of the article.)

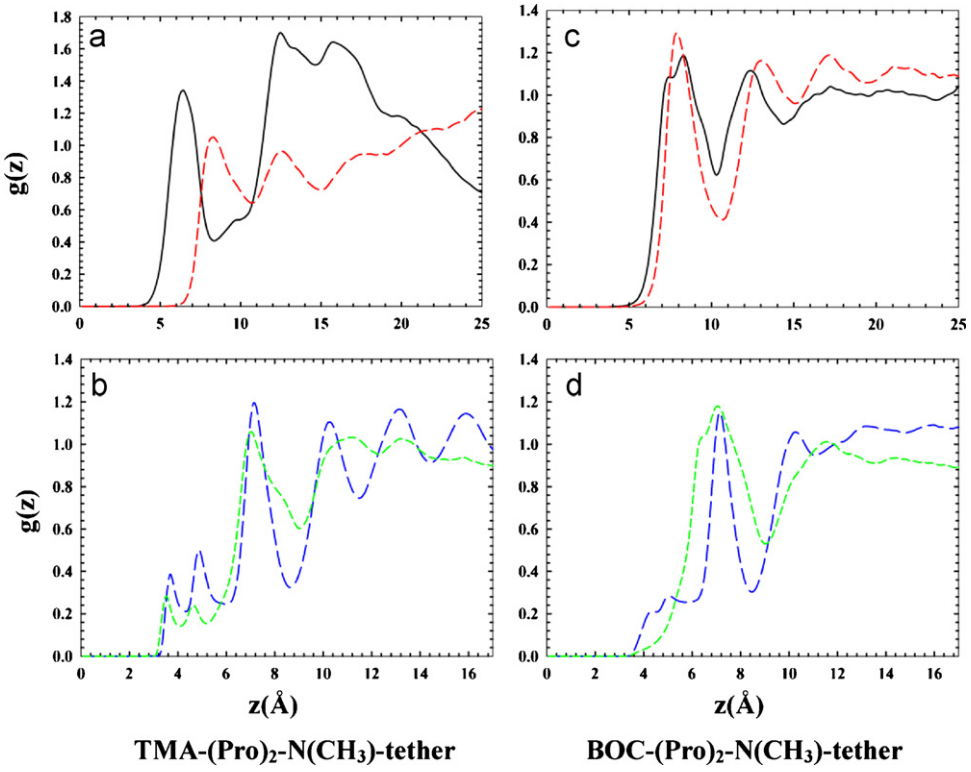

Fig. 8. Solvent distributions above the TMA-$(Pro)_2$-$N(CH_3)$-tether and the BOC-$(Pro)_2$-$N(CH_3)$-tether interfaces. Results are shown for (a) *n*-hexane/2-propanol at the TMA-$(Pro)_2$-$N(CH_3)$-tether interface, (b) water/methanol at the TMA-$(Pro)_2$-$N(CH_3)$-tether interface, (c) *n*-hexane/2-propanol at the BOC-$(Pro)_2$-$N(CH_3)$-tether interface, and (d) water/methanol at the BOC-$(Pro)_2$-$N(CH_3)$-tether interface. The surface distribution for a central carbon of *n*-hexane (red, medium dashes), the O in 2-propanol (black, solid), the O in water (blue, long dashes), and the O in methanol (green, short dashes) are shown. (For interpretation of the references to color in this figure legend, the reader is referred to the web version of the article.)

3. Results

In this section, results of molecular dynamics simulations are presented for the TMA-$(Pro)_2$-$N(CH_3)$-tether and BOC-$(Pro)_2$-$N(CH_3)$-tether chiral interfaces. Selector conformations at the interface are discussed in Section 3.1. The impact of the end-group, TMA or BOC, is evident from the comparison. Solvent distributions and hydrogen bonding at the TMA-$(Pro)_2$-$N(CH_3)$-tether and BOC-$(Pro)_2$-$N(CH_3)$-tether interfaces are discussed in Sections 2.2 and 2.3, respectively.

3.1. The structure of the TMA-$(Pro)_2$-$N(CH_3)$-tether and BOC-$(Pro)_2$-$N(CH_3)$-tether chiral interfaces

Snapshots of the TMA-$(Pro)_2$-$N(CH_3)$-tether and the BOC-$(Pro)_2$-$N(CH_3)$-tether interfaces, in the absence of solvent, in water/methanol, and in *n*-hexane/2-propanol are presented in Fig. 5. Consider first the TMA-$(Pro)_2$-$N(CH_3)$-tether interface shown in Fig. 5(e)–(h). In the absence of solvent, each selector adopts a compact structure that brings selector atoms closer to the surface. In the presence of water and methanol, some of the selectors "stretch out" into the fluid. The most extended selector conformations occur in hexane/2-propanol, as shown in Fig. 5(h) where a few selectors have their backbones roughly perpendicular to the surface. A more quantitative perspective on selector conformation is shown in Fig. 6. The distribution of backbone carbonyl carbons [C(7), C(9), and C(11)] are shown as a function of distance from the underlying silicon layer. Even for C(7), the carbonyl carbon closest to the tether and to the surface, solvent impacts the distributions, with a higher probability of being further from the silicon layer in *n*-hexane/2-propanol. The presence of solvent broadens the distribution for C(11), the carbonyl carbon closest to the terminal group. Without solvent, this carbon is found only within 5–8 Å of the underlying silicon layer but, with solvent present, C(11) can be found up-to 11–12 Å from the silicon. The probability for this extended structure is highest in *n*-hexane/2-propanol.

Snapshots of the BOC-$(Pro)_2$-$N(CH_3)$-tether interface in the absence of solvent, in water/methanol, and in *n*-hexane/2-propanol are presented in Fig. 5(a)–(d). The conformational distribution of these selectors is quite different from TMA-$(Pro)_2$-$N(CH_3)$-tether. In particular, the BOC terminated selectors have a higher probability of adopting a conformation that extends the selector along the surface. This is particularly evident in Fig. 5(b) where the solvent is absent. The presence of water/methanol encourages the selectors to extend away from the surface, but *n*-hexane/2-propanol leads to significantly more extended selector structures. Fig. 6 provides the distribution of backbone carbonyl carbons [C(7), C(9), and C(11)] as a function of distance from the underlying silicon layer. All three carbons indicate that the selectors extend furthest into the solvent for *n*-hexane/2-propanol.

A full conformational analysis of the diproline selectors was performed. These backbone preferences are shown in Table 2 and, not surprisingly, the observed conformers and their abundance are closely related to the expectations based on *ab initio* energies (see Table 1). Overall, we found that both selectors strongly favour a few conformers regardless of the solvent. However, the nature of the terminal group impacts the preference as does the solvent characteristics. We do not observe the CC conformer in the simulations but this is expected since this structure is significantly higher in energy than others. The TT, TC, and CT conformers, on the other hand, are observed at the interface. For the TMA-terminated selectors, the TT conformer is more probable than TC in accord with the expectation from *ab initio* energies. The CT conformer is higher in energy, relative to TC and TT, and is only encountered in *n*-hexane/2-propanol. The BOC-terminated selectors have different conformational preferences. The *ab initio* energies in Table 1 identify CT and TT as being

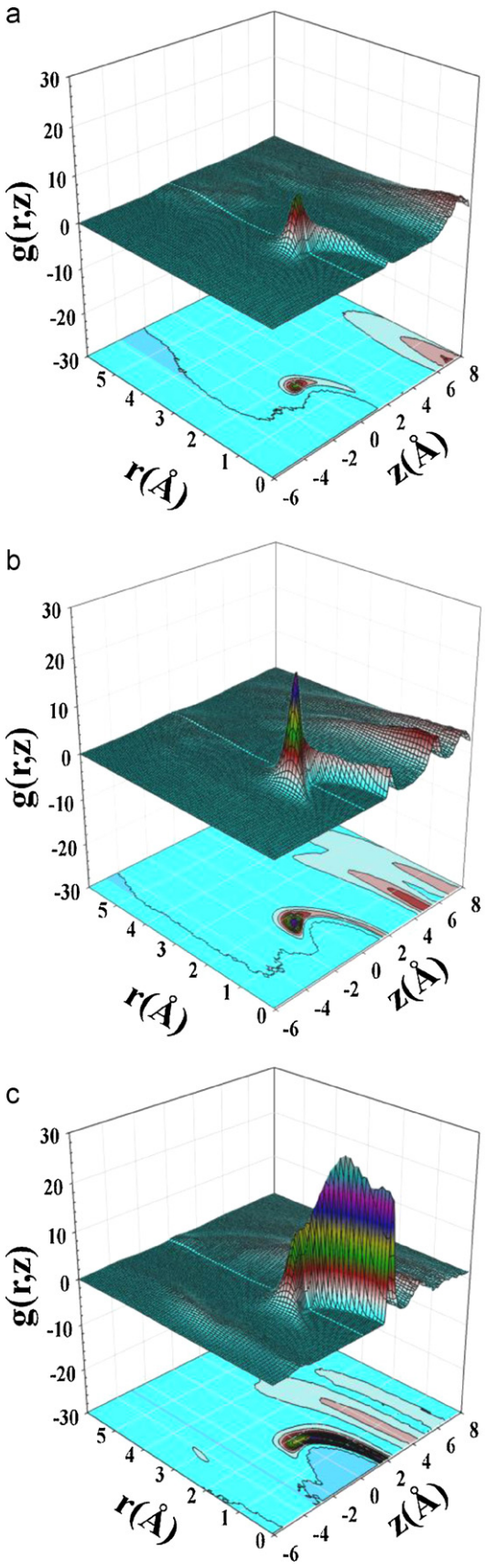

Fig. 9. The 2D distribution between the hydrogen-bonding H of 2-propanol and the carbonyl oxygens of TMA-$(Pro)_2$-$N(CH_3)$-tether for the *n*-hexane/2-propanol solvated interface. Results are given for O(8), O(10), and O(12) in (a), (b), and (c) respectively. Contour plots are also provided to highlight the locations of the features.

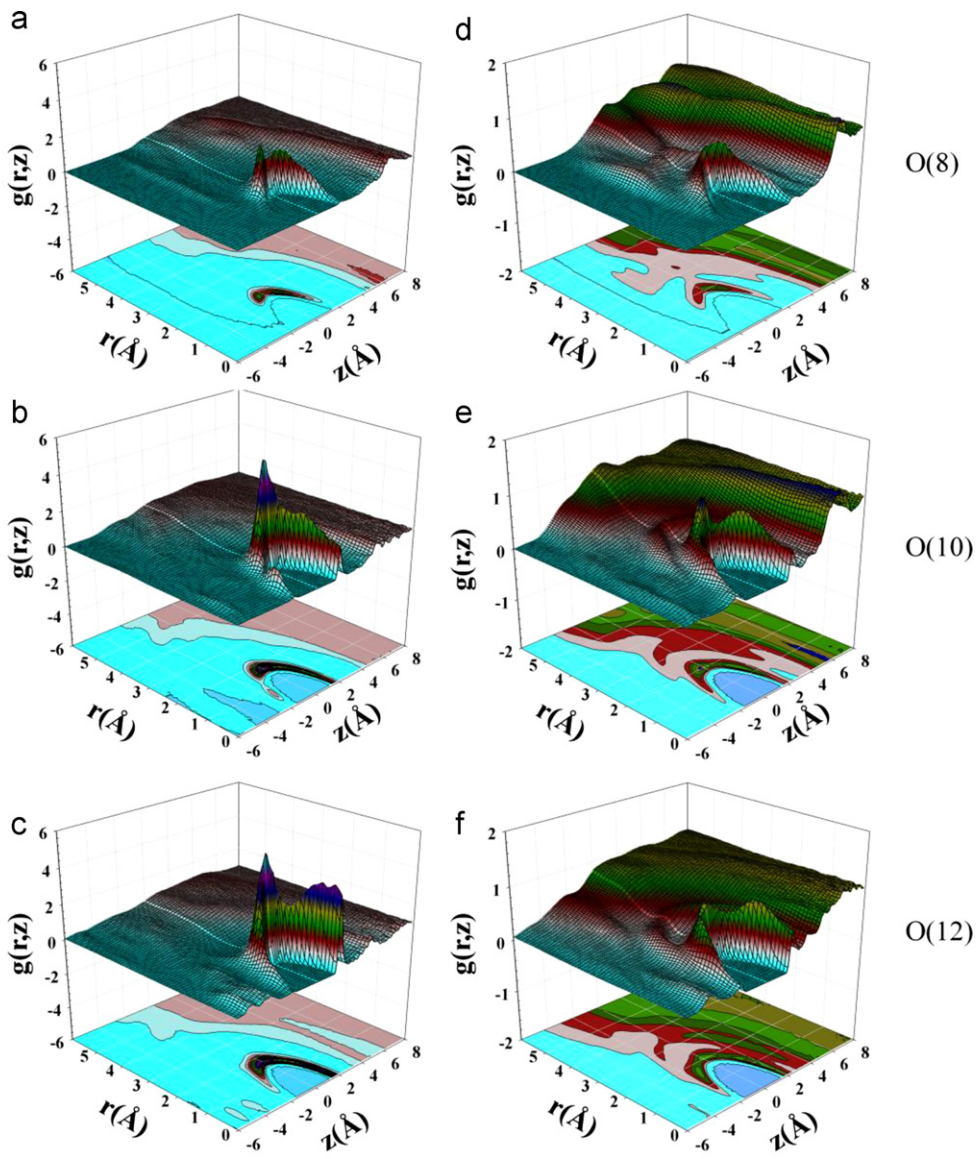

Fig. 10. The 2D distribution between the hydrogen-bonding H of methanol (a–c) and of water (d–f) and the carbonyl oxygens of TMA-$(Pro)_2$-$N(CH_3)$-tether for the water/methanol solvated interface. Results are given for O(8) in (a) and (d), O(10) in (b) and (e), and O(12) in (c) and (f). Contour plots are also provided.

very close in energy, with TC roughly 10 kJ/mol higher in energy. The simulations show that CT and TT account for over 85% of the conformations observed at the interface, with a strong preference for CT in the presence of solvent. The remaining conformers are predominantly TC.

Two additional diproline conformers identified as TG(T) and TG(C) are also observed at the surface despite being absent for a single isolated selector (see Fig. 4). TG(T) is similar to the TT conformer except that the inner amide torsion is roughly 210°, as opposed to 180° for TT. Similarly, for TG(C) the inner torsion is around 310°, as opposed to 340° for the TC conformer. These two conformers appear primarily for the TMA-terminated selectors, only when the selectors are placed at the surface, and even in the absence of solvent. In fact over two-thirds of the TMA terminated selectors adopt TC(C) when solvent is absent. The latter result signals that the TG(C) conformer results from interactions between the selectors and other surface components, such as the end-caps, silanol groups, and nearby selectors. The presence of solvent decreases the probability for TG(C), with roughly one-quarter of the TMA-terminated selectors adopting this conformation in the presence of *n*-hexane/2-propanol or water/methanol.

Orientational probabilities for the carbonyl oxygens are provided in Fig. 7. These distributions provide insight into steric hindrance that may result from the proximity of the carbonyls to the end-caps and other surface elements. Specifically, low angles correspond to a carbonyl group pointing towards the underlying surface. H-bonding to such a carbonyl may be difficult due to the presence of nearby surface elements. From Fig. 7, the TMA-terminated selectors have more variability in the orientation of the carbonyls. However, in *n*-hexane/2-propanol, the selectors clearly tend to orient O(10) towards the surface and O(8) and O(12) towards the bulk. Both selectors have similar carbonyl orientations except that the distributions are narrower for the BOC-terminated selector. In the more polar, water/methanol solvent, both selectors have a bimodal distribution for all three carbonyls with some probability of being directed at the surface and away from the surface. Again, the orientational preferences are more evident for the BOC-terminated selector.

Overall, the characteristics of the TMA-terminated and BOC-terminated selectors at the interface differ in several ways. First, the distribution of the TMA-terminated selectors is broader as demonstrated in Fig. 6, where C(11) may be found between 5 and 12 Å

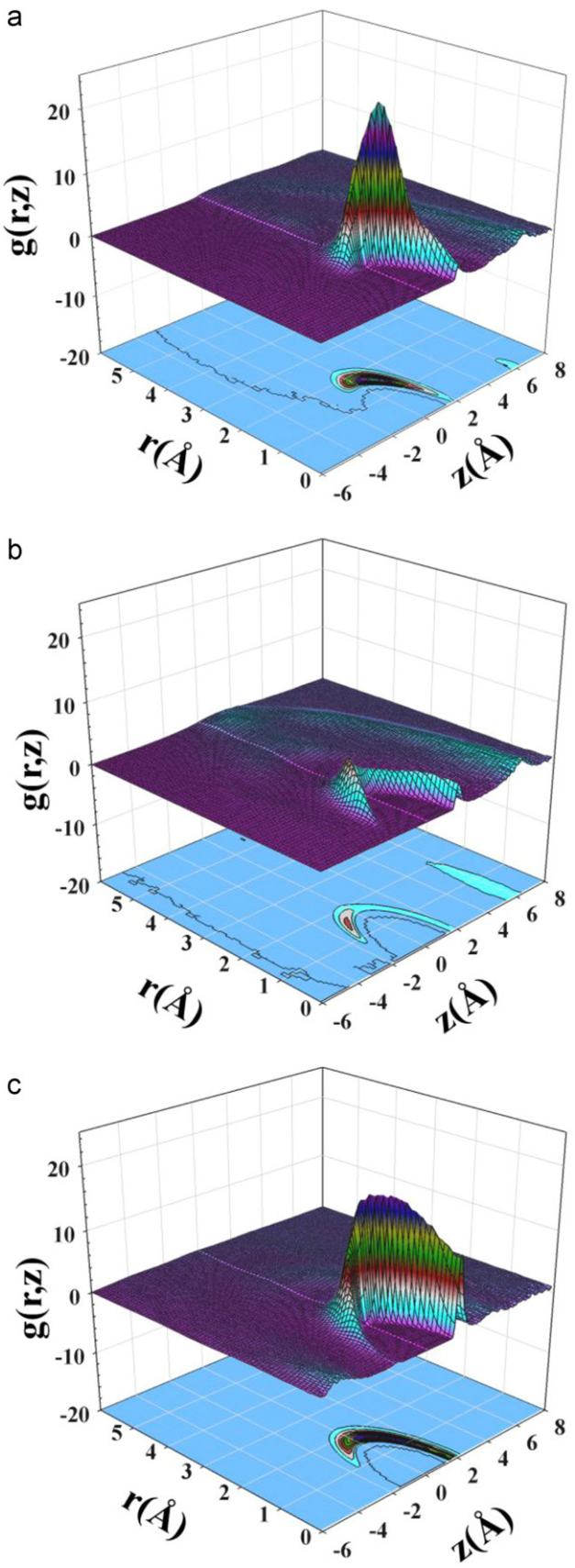

Fig. 11. The 2D distribution between the hydrogen-bonding H of 2-propanol and the carbonyl oxygens of BOC-$(Pro)_2$-$N(CH_3)$-tether for the *n*-hexane/2-propanol solvated interface. Results are given for O(8), O(10), and O(12) in (a), (b), and (c) respectively. Contour plots are also provided to highlight the locations of the features.

above the Si layer. The analysis in Table 2 and the carbonyl orientations in Fig. 7 also illustrate this conformational variability. In particular, the TG(T) and TG(C) conformers occur primarily at the TMA-$(Pro)_2$-$N(CH_3)$-tether interface. Second, the BOC-terminated selectors have a higher probability of extending along the surface, particularly in the absence of solvent. Third, the TMA-terminated selectors all prefer a trans amide bond joining the terminal TMA group to the remainder of the molecule but the amide between the rings may be either cis or trans. In contrast, the BOC-terminated selectors are consistently trans between the pyrrolidine rings but can adopt either cis or trans amides between the proline unit and the terminal BOC group.

3.2. Solvation and hydrogen bonding at the TMA-$(Pro)_2$-$N(CH_3)$-tether chiral interface

Fig. 8 provides surface distributions for the solvent at the TMA-$(Pro)_2$-$N(CH_3)$-tether interface. The distribution of *n*-hexane and 2-propanol are shown in Fig. 8(a). The alcohol distribution varies significantly at the interface, with a higher probability directly above the end-caps. At distances between 7 and 11 Å, where the bulky diprolines and terminal groups are usually located, the alcohol concentration is lower but some *n*-hexane is found. 2-Propanol is again probable beyond 11 Å where hydrogen bonding to the upper amide and to other propanols can occur. Overall, *n*-hexane prefers the bulk to the interface.

The distribution of water and methanol above the TMA-$(Pro)_2$-$N(CH_3)$-tether interface is given in Fig. 8(b). Both hydrogen-bonding solvents display similar distributions above the surface, with a higher density layer appearing at around 7 Å, followed by a low density region until around 10 Å. Beyond this distance, the solvents can hydrogen bond to an amide group or to other solvents. In the polar water/methanol solvent, the selectors have a greater propensity to adopt a TC conformation and this leads to a bent diproline conformation (see Fig. 2) that brings the proline units closer to the surface. Thus, the TC conformation excludes some solvent from the region directly above the end-caps but increases the possibility for hydrogen bonding further away from the silicon layer.

Snapshots were collected and analyzed to provide H-bonding statistics and our results are presented in Tables 3 and 4. Table 3 reports the number of selectors, with a given configuration, that have between 1 and 5 simultaneous H-bonds. For instance, at any time, the probability of having a TMA-terminated selector, in a TT conformation and with one H-bond, is 19% in *n*-hexane/2-propanol. Hydrogen bonding probability is reported as a function of the selector atom and backbone conformation in Table 4. From this table, a TMA-terminated selector in a TT conformation has a 4%, 8%, and 16% chance of having a H-bond at O(8), O(10), and O(12), respectively, in an *n*-hexane/2-propanol solvent. We do not report statistics for the nitrogen atoms in these tables, since H-bonding is almost negligible for these atoms. Table 4 also shows that H-bonding to the "extra" oxygen, O(13), in the BOC terminal group is very low. Thus, H-bonding occurs almost exclusively at the three carbonyl oxygens in the selectors.

In *n*-hexane/2-propanol, roughly one-third of all TMA-$(Pro)_2$-$N(CH_3)$-tether selectors have at least one hydrogen bond at any time. Only 6% of the selectors have more than one H-bond. This H-bonding occurs predominantly for TT conformers despite the fact that TC and TG(C) conformers account for roughly 30% of the observed selector conformers. The latter conformers are more compact and, for steric reasons, 2-propanol cannot access the carbonyl oxygens. The probabilities in Table 4 show that O(12), the oxygen nearest the terminal group, has the highest chances for H-bonding following by O(10), from the amide between the two rings.

Table 3
Hydrogen bonding statistics for the TMA-$(Pro)_2$-$N(CH_3)$-tether and BOC-$(Pro)_2$-$N(CH_3)$-tether interfaces with *n*-hexane/2-propanol and water/methanol solvents. The probability of one, or more, H-bonds as a function of conformation are given. "TT" identifies trans geometries about C(11)–N(27) and C(9)–N(21); "TC" ("CT") refers to a trans(cis) geometry about C(11)–N(27) and a cis (trans) geometry about C(9)–N(21); TG(T) and TG(C) have a trans geometry about C(11)–N(27) and a gauche geometry about C(9)–N(21) with the latter either close to cis (TG(C)) or close to trans (TG(T)).

Terminal group	Solvent	Number of H-bonds	TT	TC	CT	TG(T)	TG(C)
TMA	Water/methanol	1	**14**	**11**	0	1	**10**
		2	**14**	7	0	0	7
		3	7	3	0	0	2
		4	2	1	0	0	1
		5	1	0	0	0	0
	n-Hexane/2-propanol	1	**19**	1	2	3	5
		2	4	0	0	1	1
		3	1	0	0	0	0
BOC	Water/methanol	1	5	1	**26**	0	0
		2	4	0	**18**	0	0
		3	2	0	8	0	0
		4	1	0	0	0	0
		5	0	0	0	0	0
	n-Hexane/2-propanol	1	8	2	**16**	1	1
		2	2	0	3	1	0
		3	0	0	0	0	0

As expected, the water/methanol solvent hydrogen bonds extensively with the TMA-terminated selectors. Our simulations indicate that, at any time, roughly four-fifths of the selectors have at least one H-bond to solvent and over 45% have two-or-more H-bonds. Water accounts for over 87% of the H-bonds, as shown in Table 4, and this is due to three factors. First, the mixed solvent is 70% water. Second, water is smaller than methanol and better able to access the carbonyl oxygens in bent conformers. Finally, water can donate two H-bonds whereas methanol can only donate one. Table 3 shows that H-bonding is most probably for the TT conformer but the TC and TG(C) also contribute to H-bonding in this solvent. All three carbonyl oxygens have a significant probability to H-bond for the TT conformer. In water/methanol, the TC and TG(C) conformers also form H-bonds although O(8) is difficult to access for these conformers and, as shown in Table 4, has a lower probability to H-bond.

2D solvent distributions, $g(r,z)$, are shown in Figs. 9 and 10 for *n*-hexane/2-propanol and water/methanol, respectively, at the TMA-$(Pro)_2$-$N(CH_3)$-tether interface. The figures show the distribution between the solvent H and the carbonyl O from the selector. The ridge at roughly $r^2 + z^2 \approx 2$ Å corresponds to the H-bonding region. For O(8), the region is narrow with the H required to be equidistant ($z = 0$ Å) from the underlying Si layer. For O(10), the solvent H tends to be somewhat closer to the surface indicating that H-bonding to O(10) occurs primarily "from below". This is consistent with Fig. 7(a) where C=O(10) is most often pointed towards the surface. The uppermost carbonyl oxygen, O(12), tends to H-bond with solvent located further from the Si layer ($z > 0$ Å). As shown in Fig. 7, this oxygen is usually directed towards the bulk. The distribution for water/methanol, provided in Fig. 10, shows that the H-bonding solvents have a bi-modal H-bonding distribution, with a peak for solvent located closer to the surface and a second peak, or a shoulder, for solvent located further away. The carbonyl orientational distributions in Fig. 7 are also bimodal. Thus, the H-bonding solvent distribution is a direct result of the carbonyl orientation at the surface. It is interesting to note that the alcohols both have a depletion region beyond the H-bonding ridge. In contrast, secondary water–water interactions are evident in the 2D distributions with ridges at $r^2 + z^2 \approx 4$ Å present in Fig. 10(d)–(f).

3.3. Solvation and hydrogen bonding at the BOC-$(Pro)_2$-$N(CH_3)$-tether chiral interface

Fig. 8(c) and (d) provides surface distributions for *n*-hexane/2-propanol and water/methanol at the BOC-$(Pro)_2$-$N(CH_3)$-tether interface. These selectors strongly prefer to adopt either CT or

Table 4
Hydrogen bonding statistics for the TMA-$(Pro)_2$-$N(CH_3)$-tether and BOC-$(Pro)_2$-$N(CH_3)$-tether interfaces with *n*-hexane/2-propanol and water/methanol solvents. The H-bonding location and solvent identity, for water/methanol, are given. The probability of a hydrogen bond at the specified carbon, in the given conformer, is presented. For example, the probability of having a "TT" conformer of TMA-$(Pro)_2$-$N(CH_3)$-tether with a hydrogen bond at O(12) is 16% in *n*-hexane/2-propanol. In water/methanol, this probability is 32% with the probability for methanol given in brackets. "TT" identifies trans geometries about C(11)–N(27) and C(9)–N(21); "TC" ("CT") refers to a trans(cis) geometry about C(11)–N(27) and a cis (trans) geometry about C(9)–N(21); TG(T) and TG(C) have a trans geometry about C(11)–N(27) and a gauche geometry about C(9)–N(21) with the latter either close to cis (TG(C)) or close to trans (TG(T)).

Terminal group	Solvent	H-bonding atom	TT	TC	CT	TG(T)	TG(C)
TMA	Water/methanol	O(8)	**23** (2)	6 (1)	0	1 (0)	3 (1)
		O(10)	**19** (2)	**20** (1)	0	2 (1)	**15** (2)
		O(12)	**32** (4)	**13** (2)	0	1 (1)	**15** (2)
	n-Hexane/2-propanol	O(8)	4	1	1	1	1
		O(10)	8	1	1	1	2
		O(12)	**16**	1	1	3	4
BOC	Water/methanol	O(8)	9 (1)	1 (0)	**56** (7)	0	0
		O(10)	4 (1)	1 (0)	**19** (3)	0	0
		O(12)	8 (1)	1 (0)	**40** (6)	0	0
		O(13)	1 (0)	1	1 (0)	0	0
	n-Hexane/2-propanol	O(8)	4	2	**12**	1	0
		O(10)	2	1	2	1	0
		O(12)	7	1	8	1	0
		O(13)	1	0	1	0	0

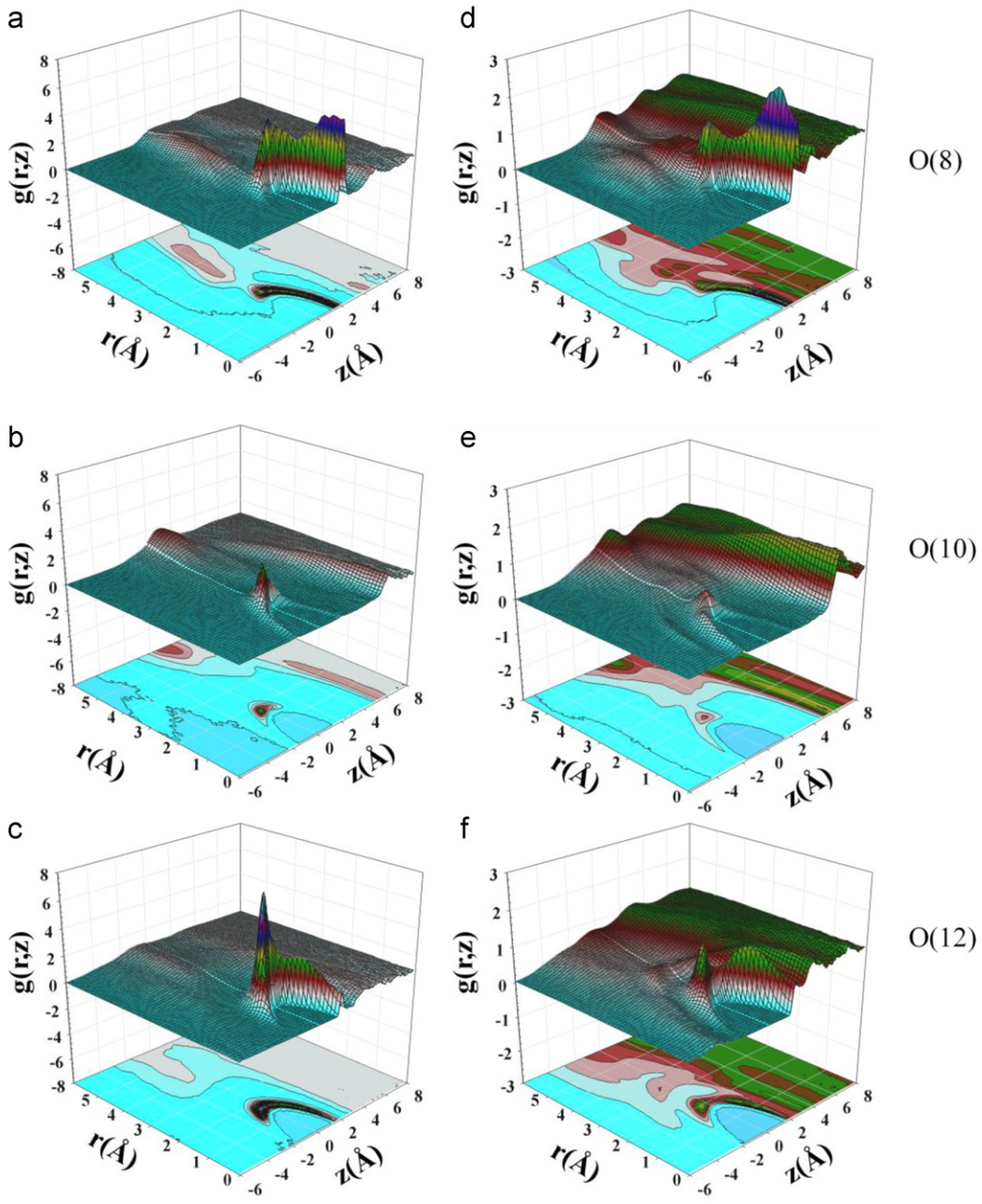

Fig. 12. The 2D distribution between the hydrogen-bonding H of methanol (a–c) and of water (d–f) and the carbonyl oxygens of BOC-$(Pro)_2$-$N(CH_3)$-tether for the water/methanol solvated interface. Results are given for O(8) in (a) and (d), O(10) in (b) and (e), and O(12) in (c) and (f). Contour plots are also provided.

TT conformations, leading to a consistently trans amide torsion between the rings and, overall, the selectors are similarly oriented at the surface. For these two reasons, the solvent distributions are simpler and less variable for the BOC-terminated selectors. Overall, *n*-hexane and 2-propanol are more concentrated between 7 and 9 Å above the Si layer, while water and methanol are found preferentially between 6 and 8 Å. As shown in Fig. 6, the selectors are more compact in water/methanol and this accounts for the shift to smaller distances. Both solvents show a depletion region at distances where the selector atoms are most often located. Directly beyond these distances, a higher solvent concentration is usually observed, but bulk distributions are quickly attained.

The BOC-terminated selectors have roughly one-third probability to H-bond in *n*-hexane/2-propanol and a much larger, four-fifths probability to H-bond in water/methanol. In the latter solvent, water accounts for over 87% of the H-bonding events. Table 3 presents the probability of finding one or more H-bonds for each conformer. Unlike the TMA-terminated selectors, H-bonding occurs most often for CT conformers. In water/methanol, there is a 26% chance of finding a CT conformer with one H-bond, and a 18% chance of finding this conformer with two H-bonds. From Table 4, all three carbonyl oxygens form H-bonds but the inter-ring oxygen, O(10), forms far fewer than O(8) and O(13).

2D solvent distributions, $g(r,z)$, are shown in Figs. 11 and 12 for *n*-hexane/2-propanol and water/methanol, respectively, at the BOC-$(Pro)_2$-$N(CH_3)$-tether interface. 2-Propanol H-bonds preferentially to O(8) and O(12) and this is evident from the peak intensity in Fig. 11(b). The inter-ring carbonyl points towards the surface, as shown in Fig. 7(c), and the 2-propanol cannot be accommodated between the carbonyl and the surface. As well, H-bonding to O(8)

occurs either from the side or from above. This is in contrast to the TMA-terminated selectors where H-bonding occurred only from the side. The 2D solvent distribution in water/methanol shows a bimodal distribution for O(8) and O(12) but only weak H-bonding to O(10). In this solvent, over 85% of the selectors adopt the bent, CT conformer with O(10) typically pointing towards the surface. With these two factors, even water cannot H-bond effectively to O(10).

4. Conclusions

Ab initio studies of BOC-$(Pro)_2$-$N(CH_3)_2$ and TMA-$(Pro)_2$-$N(CH_3)_2$ indicate that these diproline selectors have distinct conformational preferences: the TMA-terminated selector has a preference for a TT conformation but, with a BOC terminal group, CT is predicted to be the global energy minimum with TT only a few kJ/mol higher in energy. The structure and energy of the conformers was obtained with B3LYP, B97D, MP2, and MPW2PLYP-D. We find that B3LYP, MP2, and MPW2PLYP-D predict equivalent structures but B3LYP overemphasizes the energy difference between the conformers. On the other hand, B97D predicts an incorrect TC structure. Follow-up single point calculations, for the B3LYP and B97D structures, were performed at the CCSD and LPNO-CCSD levels.

An extensive series of B3LYP calculations was performed to develop molecular force fields for BOC-$(Pro)_2$-$N(CH_3)_2$ and TMA-$(Pro)_2$-$N(CH_3)_2$. The final force fields have been adjusted to reproduce conformational energies from single point CCSD/6-311G(d,p) calculations.

Each chiral selector forms the basis of an interface that also includes trimethylsilyl end-caps and silanol groups. Simulations of these interfaces have been performed in the presence of a vacuum, a 70/30 (v/v) water/methanol solvent, and a 70/30 (v/v) *n*-hexane/2-propanol solvent. Simulations in the absence of solvent identify the conformational impact of the surface environment. For the TMA-terminated selectors, surface interactions introduce two new conformations, TG(T) and TG(C), which are similar to TT and TC, but with a roughly thirty degree change in the inter-ring amide torsional angle. New surface-induced conformations do not appear for BOC terminated selectors. Overall, we find that the TMA-terminated selectors display more conformational flexibility at the interface.

Solvent alters the conformational distributions of the selectors and introduces solvent–selector H-bonding. Virtually all of the H-bonding occurs at the carbonyl oxygens: very few H-bonding events occur at the nitrogens or at the "extra" oxygen in the BOC terminal group. We find that roughly one-third of selectors have a hydrogen bond in *n*-hexane/2-propanol but roughly four-fifths H-bond in water/methanol. In the latter solvent, most of the H-bonding is between the selector and water.

For TMA-terminated selectors, H-bonding is most important for the TT conformer and all three backbone carbonyl oxygens form H-bonds with solvent. BOC-terminated selectors, in the presence of solvent, prefer the CT conformer and H-bonding occurs predominantly at O(8) and O(12). The inter-ring oxygen, O(10), is often directed towards the surface which sterically restricts H-bonding solvent.

The bent shape of the BOC-terminated selector, along with the overall inaccessibility of O(10), would not be conducive to chiral selectivity. Thus, given the different conformational and H-bonding preferences of the two selectors, it is not surprising that the selectivity depends strongly on the nature of the terminal group. Experiments [9] show that the TMA-terminated selector is superior and our simulations suggest that this is likely due to the greater accessibility of the selector to analyte. Specifically, the TT conformer of the TMA-terminated selector is extended thereby providing more interaction opportunities, particularly for hydrogen-bonding, between TMA-$(Pro)_2$-$N(CH_3)$-tether and a chiral analyte.

Acknowledgments

The financial support of the Natural Sciences and Engineering Research Council (NSERC) of Canada is gratefully acknowledged. The generous allocation of computing resources at Sharcnet, and HPCVL (High Performance Computing Virtual Lab) is gratefully acknowledged. Discussions regarding LPNO with M. Nooijen and L.M. Huntington from the University of Waterloo are gratefully acknowledged.

Appendix A. Supplementary data

Supplementary data associated with this article can be found, in the online version, at doi:10.1016/j.chroma.2011.06.096.

References

[1] J. Huang, H. Chen, T. Li, J. Chromatogr. A 1113 (2006) 109.
[2] B.W. Chellgren, T.P. Creamer, J. Am. Chem. Soc. 126 (2004) 14734.
[3] Z. Liu, K. Chen, A. Ng, Z. Shi, R.W. Woody, N.R. Kallenbach, J. Am. Chem. Soc. 126 (2004) 15141.
[4] M. Kuemin, S. Schweizer, C. Ochsenfeld, H. Wennemers, J. Am. Chem. Soc. 131 (2009) 15474.
[5] H. Zhong, H.A. Carlson, J. Chem. Theory Comput. 2 (2006) 342.
[6] B. Bochicchio, A.M. Tamburro, Chirality 14 (2002) 782.
[7] T.J. Ward, D.M. Hamburg, Anal. Chem. 76 (2004) 4635.
[8] J. Huang, P. Zhang, H. Chen, T. Li, Anal. Chem. 77 (2005) 3301.
[9] J. Huang, H. Chen, P. Zhang, T. Li, J. Chromatogr. A 1109 (2006) 307.
[10] R. Sancho, C. Minguillon, J. Chromatogr. B 875 (2008) 93.
[11] M. Li, J. Huang, T. Li, J. Chromatogr. A 1191 (2008) 199.
[12] Y. Bao, J. Huang, T. Li, D.W. Armstrong, Chromatogr. Suppl. 67 (2008) S13.
[13] W.J. Lao, J. Gan, J. Chromatogr. A 1216 (2009) 5020.
[14] W.J. Lao, J. Gan, J. Sep. Sci. 32 (2009) 2359.
[15] K.Y. Kang, J.S. John, H.S. Park, J. Phys. Chem. B 110 (2006) 17645.
[16] F. Neese, D. Liakos, A. Hansen, J. Chem. Phys. 131 (2009) 64103.
[17] F. Neese, F. Wennmohs, A. Hansen, J. Chem. Phys. 130 (2009) 114108.
[18] S. Grimme, J. Comput. Chem. 27 (2006) 1787.
[19] T. Schwabe, S. Grimme, Phys. Chem. Chem. Phys. 8 (2006) 4398.
[20] S. Grimme, F. Neese, J. Chem. Phys. 126 (2007) 124115.
[21] S. Grimme, J. Comput. Chem. 25 (2004) 1463.
[22] S. Kakinoki, Y. Hirano, M. Oka, Polym. Bull. 53 (2005) 109.
[23] S.J. Katte, T.L. Beck, J. Phys. Chem. 97 (1993) 5727.
[24] J.T. Slusher, R.D. Mountain, J. Phys. Chem. B 103 (1999) 1354.
[25] C.Y. Chemng, T.L. Chem, B.C. Wang, J. Mol. Struct. (Theochem) 577 (2002) 81.
[26] L. Zhang, L. Sun, J.I. Siepmann, M.R. Schure, J. Chromatogr. A 1079 (2005) 127.
[27] S. Nita, N.M. Cann, J.H. Horton, J. Phys. Chem. B 108 (2004) 3512.
[28] S. Nita, N.M. Cann, J.H. Horton, J. Phys. Chem. B 110 (2006) 9511.
[29] C. Zhao, N.M. Cann, J. Chromatogr. A. 1131 (2006) 110–129.
[30] S. Wang, N.M. Cann, J. Chem. Phys. 130 (2009) 244701.
[31] A.D. Rio, J.M. Hayes, M. Stein, P. Piras, C. Roussel, Chirality 16 (2004) S1.
[32] C. Altomare, A. Carotti, S. Cellamare, F. Fanelli, F. Gasparrini, C. Villani, P.A. Carrupt, B. Testa, Chirality 5 (1993) 527.
[33] T. Suzuki, S. Timofei, B.E. Iuoras, G. Uray, P. Verdino, W.M.F. Fabian, J. Chromatogr. A 922 (2001) 13.
[34] W.M.F. Fabian, W. Stampfer, M. Mazur, G. Uray, Chirality 15 (2003) 271.
[35] W. Traub, U. Shmueli, Nature 4886 (1963) 1165.
[36] P.M. Cowan, S. McGavin, Nature 4480 (1955) 501.
[37] F. Neese, ORCA, an *ab initio*, Density Functional and Semiempirical Program Package, Version 2. 8-00 , University of Bonn, Bonn, Germany, 2009.
[38] M.J. Frisch, G.W. Trucks, H.B. Schlegel, G.E. Scuseria, M.A. Robb, J.R. Cheeseman, G. Scalmani, V. Barone, B. Mennucci, G.A. Petersson, H. Nakatsuji, M. Caricato, X. Li, H.P. Hratchian, A.F. Izmaylov, J. Bloino, G. Zheng, J.L. Sonnenberg, M. Hada, M. Ehara, K. Toyota, R. Fukuda, J. Hasegawa, M. Ishida, T. Nakajima, Y. Honda, O. Kitao, H. Nakai, T. Vreven, J.A. Montgomery, Jr., J.E. Peralta, F. Ogliaro, M. Bearpark, J.J. Heyd, E. Brothers, K.N. Kudin, V.N. Staroverov, R. Kobayashi, J. Normand, K. Raghavachari, A. Rendell, J.C. Burant, S.S. Iyengar, J. Tomasi, M. Cossi, N. Rega, J.M. Millam, M. Klene, J.E. Knox, J.B. Cross, V. Bakken, C. Adamo, J. Jaramillo, R. Gomperts, R.E. Stratmann, O. Yazyev, A.J. Austin, R. Cammi, C. Pomelli, J.W. Ochterski, R.L. Martin, K. Morokuma, V.G. Zakrzewski, G.A. Voth, P. Salvador, J.J. Dannenberg, S. Dapprich, A.D. Daniels, O. Farkas, J.B. Foresman, J.V. Ortiz, J. Cioslowski, D.J. Fox, Gaussian, Inc., Wallingford, CT, 2009.
[39] H.C. Andersen, J. Comput. Phys. 52 (1983) 24.
[40] J.P. Reyckaert, A. Bellmans, Faraday Discussion Chem. Soc 66 (1978) 95.
[41] W.L. Jorgensen, J. Tirado-Rives, J. Am. Chem. Soc. 110 (1988) 1657.
[42] M.L.P. Price, D. Ostrovsky, W.L. Jorgensen, J. Comput. Chem. 22 (2001) 1340.
[43] E.M. Duffy, P.J. Kowalczyk, W.L. Jorgensen, J. Am. Chem. Soc. 115 (1993) 9271.
[44] C.M. Breneman, K.B. Wiberg, J. Comput. Chem. 11 (1990) 361.

[45] J. Nawrocki, J. Chromatogr. A 779 (1997) 29.
[46] P.E.M. Lopes, V. Murashov, M. Tazi, E. Demchuk, A.D. MacKerell Jr., J. Phys. Chem. B 110 (2006) 2782.
[47] B. Chen, J.J. Potoff, J.I. Siepmann, J. Phys. Chem. B 105 (2001) 3093.
[48] M. Levitt, M. Hirshberg, R. Sharon, K.E. Laidig, V. Daggett, J. Phys. Chem. B 101 (1997) 5051.
[49] M. Levitt, R. Sharon, Proc. Natl. Acad. Sci. 85 (1988) 7557.
[50] A. Luzar, D. Chandler, Phys. Rev. Lett. 76 (1966) 928.
[51] B.D. Smith, R. Srivastava, Thermodynamic Data for Pure Compounds , Elsevier, Amsterdam, 1986.
[52] E.J.W. Wensink, A.C. Hoffmann, P.J. van Maaren, D. van der Spoel, J. Chem. Phys. 119 (2003) 7308.
[53] P. Ewald, Ann. Phys. Lpz. 64 (1921) 253.
[54] I.C. Yeh, M.L. Berkowitz, J. Chem. Phys. 11 (1990) 3155.
[55] S. Nosé, J. Chem. Phys. 81 (1984) 511.
[56] W.G. Hoover, Phys. Rev. A 31 (1985) 1695.
[57] G.J. Martyna, D.J. Tobias, M.L. Klein, J. Chem. Phys. 101 (1994) 4177.
[58] E. Cressman, B. Das, J. Dunford, R. Ghenea, Y. Huh, S. Nita, I. Paci, S. Wang, C. Zhao, M. Ashtari, N.M. Cann, unpublished.